



Numerical Simulations of the Cosmological Axion

Max Xiao

This thesis is presented as part of the requirements for the conferral of the degree:

Bachelor of Advanced Studies (Honours)

Supervisor:
Dr. Ciaran O'Hare

The University of Sydney
School of Physics

2021

Declaration

I, *Max Xiao*, declare that this thesis is submitted in partial fulfilment of the requirements for the conferral of the degree *Bachelor of Advanced Studies (Honours)*, from the University of Sydney, is wholly my own work unless otherwise referenced or acknowledged. This document has not been submitted for qualifications at any other academic institution.

Max Xiao

November 12, 2021

Abstract

Originally designed as a solution to the strong CP problem, the QCD axion is a strong dark matter candidate as it couples to the Standard Model very weakly. The axion theory introduces a new complex scalar field which has a $U(1)_{\text{PQ}}$ rotational symmetry at high temperatures of the early Universe. However, if this $U(1)_{\text{PQ}}$ symmetry is broken after inflation, it could leave behind a network of cosmic axion strings which are topological defects and locations where the $U(1)_{\text{PQ}}$ symmetry is restored. Using numerical simulations, we study the dynamics and collapse of the highly energy dense system of axion strings. Of particular interest are oscillons which emerge at the locations of collapsed strings. Oscillons are quasi-stable objects which can only exist for a brief epoch after the QCD phase transition when the axion mass is still growing. The dynamics of axion strings and oscillons give rise to highly energetic regions which collapse into axion miniclusters which could form a large part of the dark matter abundance of our universe. By specifying certain initial conditions, we can examine and simulate strings and oscillons in isolation to better understand their behaviour. Thus, our simulations aim to give insight into the physics of these highly energetic objects which could determine how dark matter is distributed throughout the universe.

Acknowledgements

I would like to thank my supervisor Ciaran O'Hare who has been key to making this project the fun and enjoyable experience that it was. Ciaran, you have been extremely patient in dealing with my sporadic bursts of motivation to work on the project, always replying to my slack messages right away and flexible to my rescheduling of meetings. You always seem to find the time and be willing to really flesh out the subtleties of the project, making sure I do not mislead people by accident when communicating my ideas.

Brendan Harris has been a great friend and has allowed the project to run as smoothly as it did. You were willing to help me find solutions to problems in Python and actually converted me to the Church of Julia to run this project.

Zac, thanks for helping me understand axions better and teaching me about primordial black holes. Also, thanks for listening to my stupid computer science questions which have nothing to do with anything. I appreciated Archil, Dan and your feedback when it came to communicating my ideas during the presentation.

Finally, I would like to thank my family for working around my insane sleep schedule and dealing with me throughout this stressful year.

Statement of Contribution of the Student

From the dark matter projects my supervisor Dr. Ciaran O'Hare offered, I chose what I thought was the most compelling idea to explore. This was to simulate Cosmic Axion Strings and study their underlying physics and dynamics.

The cosmic strings project was conceptually demanding but the basic simulation itself was quite simple to setup. We used a grid to represent a complex scalar field and evolved it via the Leapfrog Algorithm which was suggested by my supervisor. I constructed the entire simulation myself from scratch following a Lagrangian and equations of motion [16].

My first contribution was to optimise the code so it ran more efficiently. To do this, I actually switched programming languages to Julia so I could take advantage of its just-in-time compilation and multi-threading capabilities. I used mutating functions and also changed arrays to update element-wise. This was a more efficient method of allocating memory which significantly reduces computation times as array size increases. This helped Giovanni Pierobon, a PHD student at UNSW, who also works on cosmic string simulations with my supervisor Ciaran O'Hare and the UNSW team.

My supervisor mainly guided me on what physical quantities may be of interest. I was able to design ways to visualise and plot the data such as energy density in 2D and 3D, and analyse it using Fourier transforms. I also designed a string finding algorithm using image processing techniques. This was later replaced by another algorithm designed by Giovanni as it could be implemented in the 3D simulations. All the visualisations of fields and power spectrum plots in this thesis are my own work. I also designed the initial conditions for the attractor string solution myself to explore the dynamics of strings.

This project was very theoretical in its nature. I used computer simulations to create data and analysed it myself.

Statement of COVID-19 Impact

COVID-19 meant that I had to adapt to a change in working environment. Instead of working on campus, I would be working from home. However, all meetings with my supervisor or at Journal clubs still continued as normal with the exception that it was all on Zoom. My project being computational in nature went on unimpeded and I kept in regular contact with my supervisor over Slack and the rest of the particle physics group. I actually found it easier to contribute in the weekly Journal clubs, and talk about the papers I found on Bentz-fields. Overall, working at home due to COVID-19 has not majorly affected my project though it has been a challenge to continually make consistent progress.

Contents

Abstract	iii
Acknowledgements	iv
Statement of Contribution of the Student	v
Statement of COVID-19 Impact	vi
List of Figures	viii
1 Introduction	1
1.1 Motivation	1
1.2 Strong CP Problem	1
1.3 Complex PQ Scalar	2
1.4 QCD Axion	5
1.5 Axion-Like Particles	6
1.6 Dark Matter	7
1.7 Axions as Dark Matter	8
2 Simulation Setup	9
2.1 Broken Before Inflation	9
2.2 Broken After Inflation	9
2.3 Setup	9
2.4 Equations of Motion	11
2.5 PQ Epoch	12
2.6 QCD Epoch	12
3 Results	14
3.1 PQ Epoch	14
3.2 QCD Epoch	17
3.3 String Dynamics	21
3.4 Opposite Chirality Strings	22
3.5 Oscillons	25
3.6 Manufactured Oscillons	27
4 Implications	29
4.1 Detection	29
4.2 Future Research	30
5 Conclusion	33
A Appendix	34
Bibliography	35

List of Figures

1.1	Neutron electric dipole moment	2
1.2	Breaking of $U(1)_{\text{PQ}}$ symmetry to attain a non-zero VEV	2
1.3	Strings as topological defects	3
1.4	Strings in the simulations	3
1.5	Tilted potential due to coupling to QCD	4
1.6	Axion potential after QCD phase transition for a different model	4
1.7	Parameter space for the axion in terms of axion-photon coupling	6
1.8	Bullet Cluster evidence for dark matter	8
3.1	Starting and finishing points of the PQ Epoch	14
3.2	Number of strings in the PQ simulation	15
3.3	Power spectrum of the saxion field for the PQ epoch	16
3.4	Power spectrum of the axion field for the PQ epoch	16
3.5	Power spectrum of the saxion field for different axion masses	17
3.6	Power spectrum of the axion field for different axion masses	17
3.7	Power spectrum of the saxion field for different λ	18
3.8	Power spectrum of the axion field for different λ	18
3.9	Number of strings for the QCD simulations when changing axion mass and λ	19
3.10	Number of strings in the QCD simulation for different couplings to QCD	19
3.11	Power spectrum of the saxion field for different couplings to QCD	20
3.12	Power spectrum for the axion field for different couplings to QCD	20
3.13	Power spectra to identify the collapse of the axion string network	21
3.14	Collapse of the axion string network for different simulations	21
3.15	Strings and domain walls as locations of high energy density	22
3.16	Strings of opposite chirality	22
3.17	4 string stable configuration	23
3.18	Starting point for a simulation with 12 strings	23
3.19	Unnatural String Configuration	24
3.20	Strings of opposite chirality attract	24
3.21	An image of oscillons in the field	25
3.22	Energy density plot of the field for a lighter axion mass	26
3.23	Energy density plot of the field for an axion mass	26
3.24	Energy density plot of the field for a heavier axion mass	27
3.25	Comparing overdensities from oscillons for different axion masses	28
4.1	Axion-photon interaction induced by an external magnetic field	29
4.2	Y-junction formation in 3D	31
4.3	Axion parameter space with an additional companion axion	32

Chapter 1

Introduction

1.1 Motivation

The Standard Model (SM) of particle physics has had many successes. A recent success of the SM was in 2012, when the Large Hadron Collider at CERN confirmed the existence of the long-awaited Higgs boson [4]. This was a particle predicted as a result of the Higgs mechanism proposed by Peter Higgs in 1964 to explain why some particles have mass [34]. The SM describes how regular matter is made up of smaller constituents, such as quarks and leptons, and how gauge bosons mediate the forces between them. Despite its predictive capabilities, the SM remains incomplete. Most notably, the SM does not provide a theory for gravity nor does it provide a particle candidate for dark matter which is required to explain cosmological processes such as galaxy formation that regular matter cannot. However, as Weinberg said, "Physics thrives on crisis" [68].

We extend the SM by including the axion which was a scalar particle originally designed to solve the strong charge parity (CP) problem. It addresses a discrepancy of Quantum Chromodynamics (QCD), the theory that explains the strong force, which cannot explain why CP is conserved in strong interactions. Not only does the axion solve the strong CP problem, it is potentially a very good dark matter candidate. We use numerical simulations to explore the consequences on the dark matter distribution of the Universe if axions are dark matter. Given the simplicity of the axion model, we are able to study the effects of both the QCD axion and axion-like particles which appear in UV complete theories such as string theory which aim to provide a theory of quantum gravity [21]. We simulate the evolution of an axion field through the early Universe and examine how it can affect our current understanding of cosmology.

1.2 Strong CP Problem

The QCD axion arises from a theory designed by Peccei and Quinn (PQ) [55] which was made to solve the strong CP problem. Unlike the weak interaction, the strong force, as far as we have measured it, does not violate CP symmetry. This is surprising because our current understanding of QCD predicts that CP symmetry should be violated by the structure of the QCD vacuum [55].

The CP conserving nature of the strong force can be seen in the electric dipole moment of the neutron in figure 1.1. There is seemingly no reason why the quarks are arranged in a configuration such that $\langle \theta \rangle = 0$ in the SM. Even the anthropic principle cannot be used to explain why the strong force seems to enforce CP symmetry [36]. This suggests that some sort of ‘fifth force’ may be at play as it cannot be explained by our current understanding of the four fundamental forces. The predicted value from one-loop approximations in QCD suggests that the neutron dipole moment should be around $|\mathbf{d}| = 1.42 \times 10^{-16} \bar{\theta} e \cdot \text{cm}$ [45]. Experiments have consistently measured an upper limit on the neutron dipole moment to be $|\mathbf{d}| < 1.8 \times 10^{-26} e \cdot \text{cm}$ [6]. This means the average angle θ for the quark arrangement in figure 1.1 is $\bar{\theta} \lesssim 10^{-10}$.

$$\mathcal{L}_{\text{QCD}} = \frac{\theta}{32\pi^2} \text{Tr } G_{\mu\nu} \tilde{G}^{\mu\nu} \quad (1.1)$$

The QCD Lagrangian in equation 1.1 violates CP symmetry unless the θ is set to zero. Rather than taking θ as a constant as per the SM, the axion theory introduces a new field $a(t, x)$ for which $\theta = a(t, x)/f_a$, where f_a

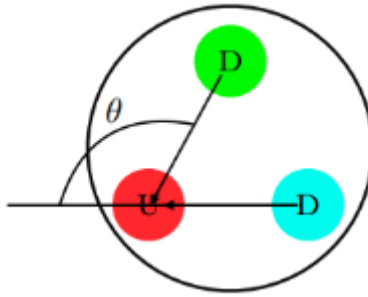


Figure 1.1: Classical picture of the neutron electric dipole moment [36]. Given that the up quark has an electric charge of $2/3e$ and the down quarks each have an electric charge of $-1/3e$, their arrangement should provide a net electric dipole moment. There is seemingly no physical reason why the experimentally observed value of $\theta \lesssim 10^{-10}$ is so low.

is the axion decay constant. This axion field has a potential which dynamically relaxes the value of θ to zero or cancels the angle enough that CP symmetry is seemingly conserved [17].

1.3 Complex PQ Scalar

PQ introduces the complex scalar field $\psi = re^{ia/f_a}$ which couples to the gluon field to solve the strong CP problem and other SM couplings depending on the model. $r(x, t)$ is introduced as the radial mode which is the saxion, and $a(x, t) = \theta f_a$ is the angular mode of the field which is the axion. This ψ field is taken to be invariant under a global $U(1)_{\text{PQ}}$ Peccei-Quinn axial (rotational) symmetry. The potential of ψ is dynamic and evolves over time according to the temperature profile of the Universe as seen in figure 1.2. On the left, a $U(1)_{\text{PQ}}$ symmetry is evident in all particle interactions in the early universe. However, a phase transition spontaneously breaks this PQ symmetry when the temperature of the Universe cools so that $T \lesssim f_a$. f_a is the scale of spontaneous symmetry breaking which can occur before or after the inflationary epoch which is assumed to occur 10^{-36} to 10^{-32} seconds after the Big Bang [59]. This results in the so-called ‘Mexican hat potential’ on the right. After this point, the ψ field develops a non-zero vacuum expectation value (VEV) which has a residual shift symmetry of $a \rightarrow a + 2n\pi f_a$. The axion is the angular degree of freedom for the VEV, where no particular value of $\theta \in (-\pi, \pi]$ is favoured.

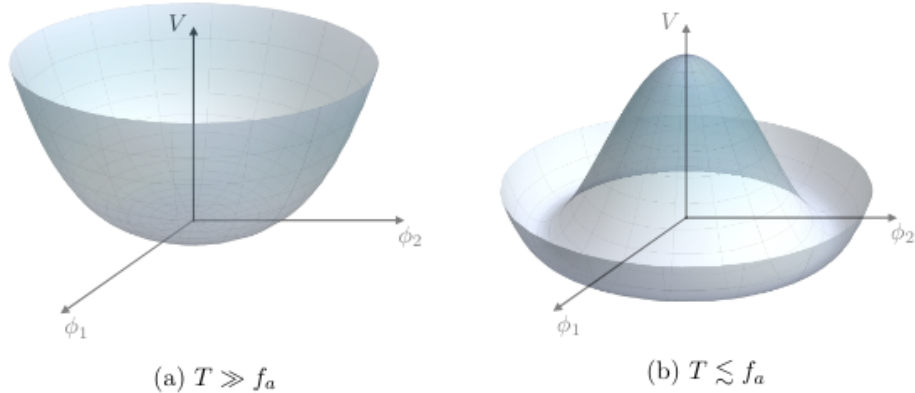


Figure 1.2: At large temperatures of the early Universe (left), the potential is $U(1)_{\text{PQ}}$ symmetric. PQ symmetry is broken (right) when the temperature falls such that $T \lesssim f_a$, allowing the potential to attain a non-zero VEV. The VEV of the radial mode is $f_a/\sqrt{2}$ in the Peccei-Quinn-Weinberg-Wilczek model [47]. This image was made by Giovanni Pierobon.

When certain symmetries are broken during a phase transition, it may be possible that topological defects form. Topological defects are stable configurations of matter which are a consequence of geometry. Whilst the rest of the field takes up θ values such that there is a continuous change in θ as one moves across the

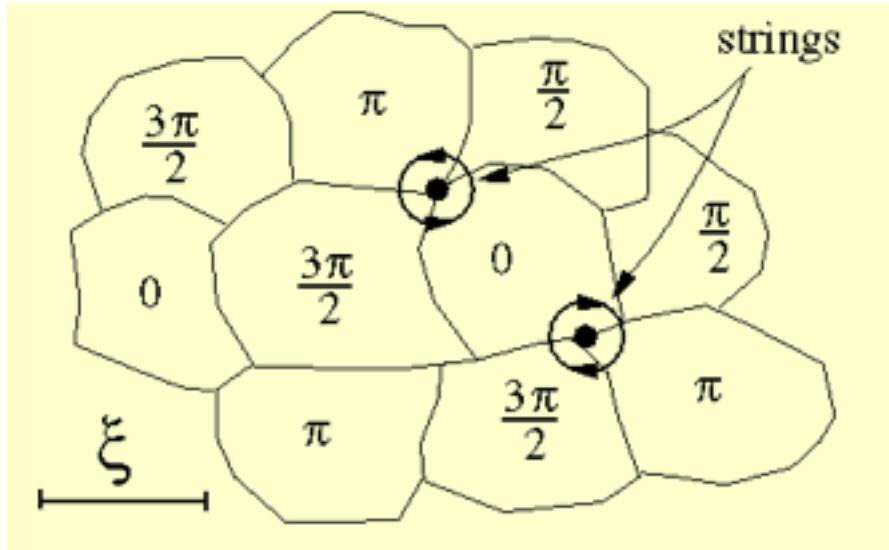


Figure 1.3: Strings are locations where there is a discontinuous change in θ . This forces the field values to the top of the potential in figure 1.2 where $U(1)_{\text{PQ}}$ symmetry is restored. [2]

field, certain points appear in the field that cannot take up one of those values as seen in figure 1.3. Cosmic strings appear as a consequence of this geometry as in figure 1.4. Strings are points where $U(1)_{\text{PQ}}$ symmetry is restored as field points all around it taken up values spanning the entire θ domain from $-\pi$ to π .

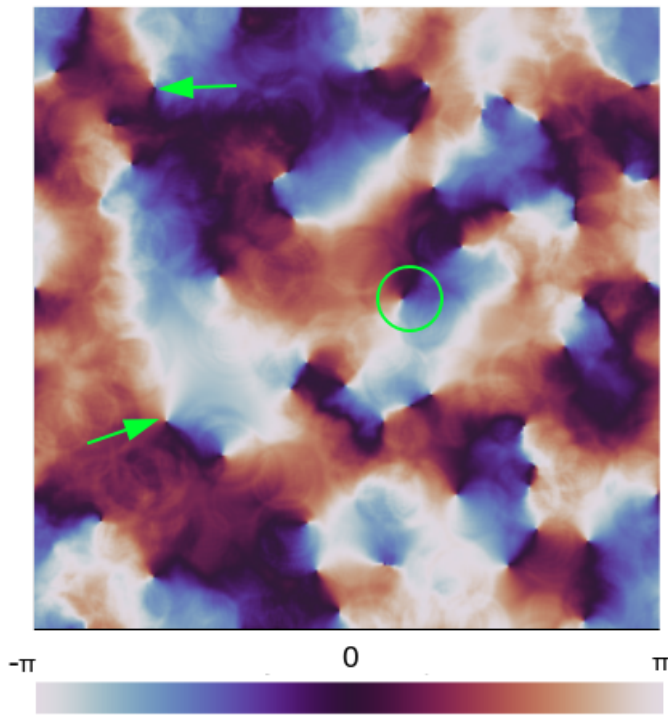


Figure 1.4: An image of the angular component of the ψ field during a snapshot in the QCD epoch. A cyclic colour map is used because the θ takes on values of a circle. This means the colour of $\theta = -\pi$ and $\theta = \pi$ are the same. Strings can be identified as regions where the surrounding lattice points span the entire cyclic colour map. Some string locations have been circled and pointed out.

Normally $a(x, t)$ would represent a Goldstone boson for which $a \in (-\pi f_a, \pi f_a]$. The axion particle, being massless would travel at c . However, to solve the strong CP problem, the axion must couple to QCD. By design, axion couplings to the SM $g \propto 1/f_a$ are suppressed by the scale f_a . f_a is extremely large, comparable to high temperatures of the early Universe only fractions of a second after the Big Bang. Because the axion weakly couples to QCD, it does not interfere with our current understanding of physics in the early Universe. If the

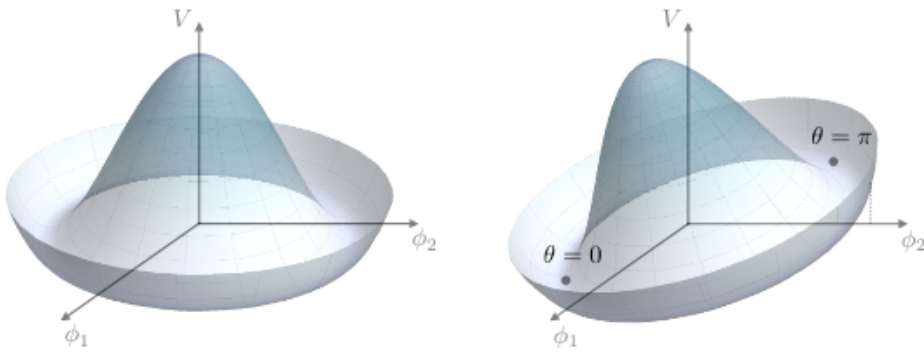


Figure 1.5: During the QCD phase transition $10^{-5}\text{s} \sim 1\text{s}$ after the Big Bang, the axion potential begins to ‘tilt’ due to the axion’s coupling to QCD. The tilt of the potential is temperature dependent and only becomes relevant when $T \sim \Lambda_{\text{QCD}}$. This is the confinement scale where quarks become bound into hadrons and when QCD effects need to be considered. This image was made by Giovanni Pierobon.

axion couples too strongly to QCD, the abundance of ^4He produced during Big Bang Nucleosynthesis will be much lower compared to what is experimentally observed [13]. Coupling to QCD causes the axion potential to ‘tilt’ such that a roughly quadratic potential is created in the angular part of the field, driving θ to 0 as seen in figure 1.5. This breaks the residual shift symmetry and generates the axion a small mass, making the axion a pseudo Nambu Goldstone Boson.

The ‘tilt’ of the potential also creates a new minimum for the ‘Mexican hat potential’ at $\theta = 0$ for the angular part of the field. However, as a result of symmetry breaking, domain walls are topological defects which appear and can be explained by figure 1.5 as locations where the angular mode of the field is stuck at the $\theta = \pi$ saddle point.

Domain walls, if they persist throughout the age of the Universe until today, are disastrous. This is because they have an equation of state of $\omega_{\text{walls}} = -2/3$. This leads the energy density of domain walls to dilute as $\rho_{\text{walls}} \sim R^{-1}$, where R is the scale factor [28]. This is a much slower rate than what radiation (which follows R^{-4}) and matter (which goes by R^{-3}) follow. Hence, domain walls will quickly dominate the energy density of the Universe. Thus, we require some mechanism by which domain walls are made unstable. For the case in our simulations, there is only one domain wall ($N_{\text{DW}} = 1$) at $\theta = \pi$. When the axion begins to couple to QCD, axion strings become the boundary of domain walls. When these strings collide, domain walls are ‘unzipped’, and the energy stored within them will be released as barely relativistic axions [61]. When more than one vacuum appears in the axion potential as seen in figure 1.6, which is the case for DFSZ model we will elaborate on later, the number of domain walls is greater than one ($N_{\text{DW}} > 1$). In this scenario, some other mechanism must remove domain walls (see Ref [41]). Our simulations only explore the $N_{\text{DW}} = 1$ case.

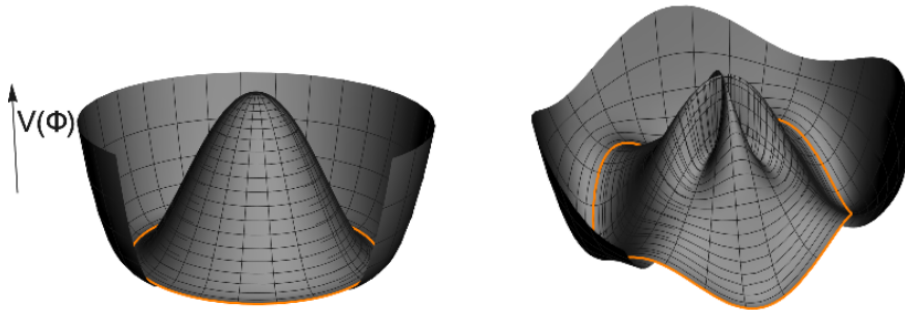


Figure 1.6: ‘Mexican hat potential’ before (left) and after (right) the QCD phase transition. In this model, $N_{\text{DW}} = 4$ is chosen [17].

1.4 QCD Axion

The mass of the QCD axion is given by

$$m_{a,\text{QCD}} \approx 6 \times 10^{-6} \text{ eV} \left(\frac{10^{12} \text{ GeV}}{f_a/\mathcal{C}} \right) \quad (1.2)$$

which has been predicted to be around 50 - 1500 μeV based on high temperature QCD lattice simulations [14]. The axion has a small mass due to its weak coupling to QCD. The QCD axion also weakly couples to SM particles and eventually becomes non-relativistic, making it ‘cold’. As consequence it is a great dark matter candidate as it provides an invisible form of matter that has so far evaded detection.

It is important to note that the mass of the QCD axion m_a is related to the axion decay constant f_a by $m_a \sim 1/f_a$. This is why the QCD band represented in figure 1.7 is only that specific narrow yellow strip. However, equation 1.2 only represents the zero-temperature mass, which is used to describe axion mass for the low temperature current Universe. During the QCD phase transition, the axion’s coupling to QCD gradually increases, raising the axion mass from zero until its zero-temperature mass as seen in equation 1.3.

The axion mass for a general axion model is parametrised by [16]

$$m_a(T)^2 = \min \left[\frac{\alpha_a \Lambda^4}{f_a^2 (T/\Lambda)^n}, m_a \right], \quad (1.3)$$

where $\Lambda = 400 \text{ MeV}$ is the QCD scale, $\Lambda = 400 \text{ MeV}$ and $n = 6.68$. n is the value of the power-law from the dilute instanton gas model which determines how strongly coupled the QCD axion is to the strong force [67]. n is a parameter which describes the axion’s strength of coupling to QCD. So for axion-like particles which we will discuss in the next section, n will not be 6.68. Thus, in our simulations, n is taken as a free parameter. $\alpha = 1.68 \cdot 10^{-7}$ is the coefficient as a result of the model. m_a is the zero-temperature axion mass which would be the observed axion mass today. The zero-temperature axion mass is given by

$$m_a^2 = \frac{m_\pi^2 f_\pi^2}{f_a^2} \frac{m_u m_d}{(m_u + m_d)^2}, \quad (1.4)$$

where m_π is the pion mass, f_π is the pion decay constant, $m_{u/d}$ is the up/down quark mass.

Because QCD axion is well motivated as a theory, we focus on the QCD axion in our simulations. There are three main QCD axion models,

- Peccei-Quinn-Weinberg-Wilczek (PQWW) axion [54], it is the simplest extension to the SM and introduces only the single additional complex scalar field tied to the electroweak Higgs sector which sets $f_a \approx 250 \text{ GeV}$. f_a is small and so the axion couplings $g \sim 1/f_a$ are large. The PQWW model is excluded by beam dump experiments [43] and by the Large Electron-Positron collider experiment which observe a lower than expected photon flux from the axion-photon interactions [48]. Unlike the PQWW model, the KSVZ and DFSZ treat f_a as a free parameter to avoid being excluded by experiment.
- Kim-Shifman-Vainshtein-Zakharov (KSVZ) axion [42], which introduces additional heavy quarks and the additional complex scalar. This model expands on the PQWW model by making the axion ‘invisible’. This protects the axion from the constraints from collider experiments to explain why the PQWW axion has not been found.
- Dine-Fischler-Srednicki-Zhitnitsky (DFSZ) axion [23], introduces an additional Higgs field and the complex scalar. Some DFSZ models predicts a superconducting string, leading to novel new string Physics not explored in this simulation [5].

These models predict different couplings, though the axion mass which is dependent on f_a remains a free parameter for the KSVZ and DFSZ models. This can be explored and probed through our simulations. They generally line up with the yellow QCD band in figure 1.7. We explore an effective KSVZ axion model in our simulations as we choose $N_{\text{DW}} = 1$. The mass of the QCD axion is treated as a free parameter which is determined by our choice of the axion decay constant f_a .

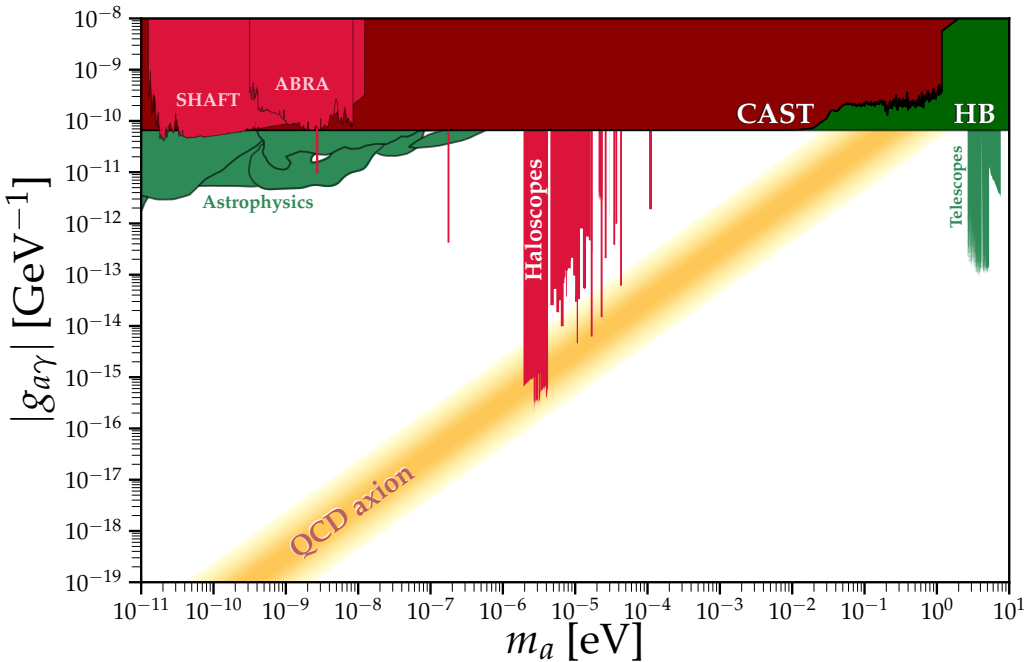


Figure 1.7: This is the axion parameter space probed by experiments relying on the axion-photon coupling $g_{a\gamma}$. The large horizontal red coloured region at the top of the plot are excluded by light-shining-through-walls experiments and solar axion searches. The narrow vertical bands are dark matter haloscope searches. Dark matter haloscopes, unlike other experiments, assume that axions are dark matter. The narrow yellow strip is the axion predicted by QCD axion models [51].

1.5 Axion-Like Particles

Another reason why the axion is compelling is that it is a simple theory. It hypothesises a spin 0 pseudoscalar particle which has its $U(1)_{\text{PQ}}$ symmetry broken as the Universe cools. The discovery of the Higgs boson has motivated a whole host of theories as its existence as the only spin 0 scalar particle in the SM validated the possibility that other spin 0 scalar particles are yet to be discovered.

From here on, ALPs describe a scalar particle which do not solve the strong CP problem. They are defined in figure 1.7 as axion models that do not coincide with the QCD axion band. For ALPs, the axion mass m_a and the axion decay constant f_a can be independent of each other, depending on the model. This is different to the QCD axion scenario in equation 1.2 where axion mass is dependent on f_a . Much of the phenomenology and cosmology as a consequence of the QCD axion is shared by the wider class of ALPs. For our simulations, the only change is that two free parameters must be chosen for an ALP model rather than just the singular parameter for the QCD axion.

An axion in string theory is a more general term to refer to pseudoscalar matter fields that become available due to additional compactified spatial dimensions [63]. These axions, though inspired by the QCD axion, do not solve the strong CP problem and are ALPs. In string theory, it is natural to expect a large number N of ALPs that interact with the SM. A linear combination of these ALPs may couple to QCD and solve the strong CP problem [22]. This leaves $N - 1$ ALPs left to form the dark matter abundance of the Universe.

From the perspective of a string theorist, the QCD axion could just be another subset of axion admitted by string theory. Furthermore, both the QCD axion and ALPs from string theory could be dark matter. Thus, the QCD axion and axion-like particle are well motivated and could be a result from higher energy theories which have not yet been explored at colliders, which collides protons at up to 13 TeV [3]. These experiments currently are not able to probe higher energies such as the $f_a = 10^{15}$ GeV used in our axion simulations. Dark matter haloscope experiments such as ADMX and HAYSTAC in the vertical red shaded region of figure 1.7 are currently in operation to detect axions if they are indeed dark matter [40, 24]. Even if the search in the QCD axion band in figure 1.7 provides a null result, perhaps experiments may detect an ALP, which will provide evidence possibly supporting a type of string theory and pointing to new Physics.

Axions in the mass range of 10^{-33} eV $\lesssim m_a \lesssim 10^{-18}$ eV are generally referred ultralight axions (ULAs).

ULAs have emerged as a possible form of dark matter to address the cold dark matter ‘small scale crises’ [47]. The ‘small scale crises’ can be summarised as the predicted overabundance of small scale dark matter structure compared to what is observed [49].

ULAs are also strong inflaton candidates as they can facilitate a mechanism for a period of accelerated expansion in the early Universe. However, since the inflaton must decay, an axion driving inflation cannot also be a dark matter candidate or solve the strong CP problem [47]. Interestingly, simulations of a scalar inflaton field by Eggemeier et al. [27] have explored mechanisms whereby the energy-density of the inflaton field can be converted to SM particles and dark matter.

Thus, both the QCD axion and ALPs are quite well motivated. Through our simulations, we can study the effects of both cases on the dark matter distribution of our Universe if they are to be at least of a fraction of the dark matter abundance.

1.6 Dark Matter

Dark matter is a hypothetical form of matter which has become central to modern cosmology. Many astrophysical gravitational interactions can only be explained via a modified theory of gravity or the existence of unseen matter providing the necessary mass to facilitate the observed behaviour of celestial objects [11]. Dark matter is essentially matter which does not or only very weakly interacts via the electromagnetic field, which explains why it has eluded direct detection [60]. We have abundant evidence from many astrophysical probes that infer that dark matter is actually the dominant form of matter in our Universe.

Baryonic matter is used by cosmologists to refer to matter which is not dark matter. The Cosmic Microwave Background (CMB) provides a good indicator of the amount of baryonic matter in our universe. The light from the CMB is essentially the light from the moment when radiation became decoupled with baryonic matter, about 380,000 years after the Big Bang [35]. These background photons have survived until today and their wavelengths have become redshifted to microwave ranges due to the expansion of the Universe. The resultant power spectrum of the temperature fluctuations tell us that if baryonic matter makes up 5% of the universe’s energy budget [66], then the correct mass distribution of 4He , 2H and 7Li are predicted from the Big Bang Nucleosynthesis [10]. This is a clear indicator that dark matter is non-baryonic. If dark matter was baryonic, the CMB would look radically different to what is observed [56]. Thus, theories of new particles beyond the SM are required to explain the nature of dark matter. These particles had to exist before BBN in order to reproduce these observations.

By looking at galaxies, we can observe the motion of baryonic matter. However, baryonic matter near the edges of galaxies are travelling much too fast according to our current understanding of gravity [7]. Just from looking at the Milky Way, we see an interesting rotation curve for celestial objects as we move radially outwards from the galactic centre. These rotation curves imply that the distribution of dark matter is roughly isotropic and spherically symmetric in the form of a halo [62]. For our Milky Way, the dark halo has a radius that appears to extend for ~ 100 kpc from the galactic centre [69]. Furthermore, galaxy formation in the early Universe difficult for baryonic matter which is affected by radiation [50]. The matter density perturbations that collapse into stars and galaxies do not grow in the radiation dominated periods of the early Universe [38]. Hence, given the observed abundance of baryonic matter in the Universe, there is seemingly not enough time for the formation of early galaxies. This suggests the existence of dark matter which is unaffected or is only weakly affected by radiation [60] which can provide a mechanism for accelerating and allowing for structure formation.

The Bullet Cluster is the most visually striking piece of evidence for dark matter. It is the result of two galaxy clusters and their halos colliding. The dark matter of these galaxies indirectly detected by gravitational lensing seemed to pass through each other. However, the baryonic matter or hot gases interacted electromagnetically, slowing them down and emitting X-rays. This allowed a clear separation of baryonic and dark matter to be seen as depicted in figure 1.8. This cannot be explained without a theory of modified gravity or the admission that the majority of mass in the system is unseen [20].

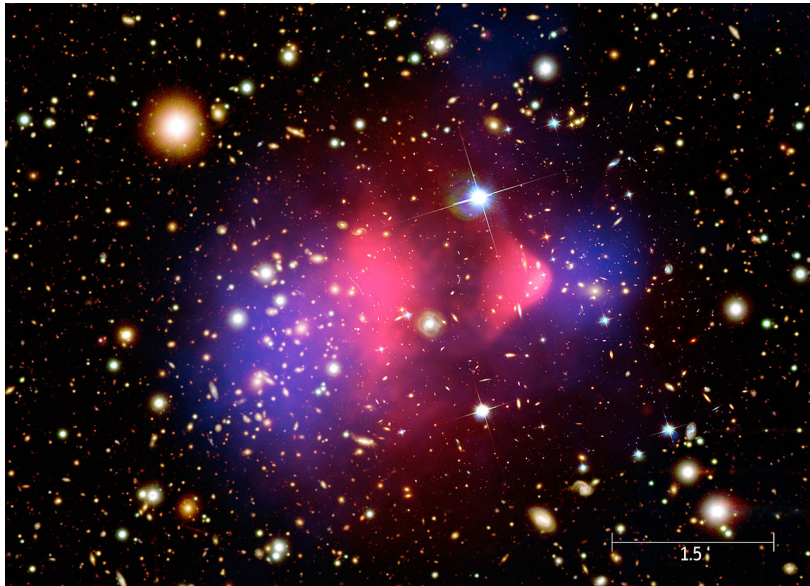


Figure 1.8: The Bullet Cluster is a result of two galaxies colliding with each other. The dark matter distribution of galaxies is shown in blue whilst the X-ray signals identifying the hot baryonic gases interacting via the electromagnetic force are shown in pink. A clear separation between dark and baryonic matter can be observed. This aligns with predictions that dark matter primarily interacts gravitationally [1].

1.7 Axions as Dark Matter

Current measurements of the local dark matter density near our Sun is $0.2 - 0.56 \text{ GeV} \cdot \text{cm}^{-3}$ [58]. If the axion were to be dark matter, given that the axion mass is very light, the number of axions per Hubble volume to make up the observed dark matter density would be extremely large. Axions by definition are bosons and hence they do not follow the Pauli Exclusion Principle that would exclude a fermion of the same mass as dark matter. This leads to high occupation numbers leading to a scenario where the axions are highly degenerate and collectively behave like a classical field. The density of axions can be interpreted as the amplitude of oscillation of the axion field. The frequency of oscillation is given by the axion coupling to QCD and the amplitude of oscillation sets the energy density.

If the $U(1)_{\text{PQ}}$ symmetry is broken after inflation, a network of cosmic axion strings will be left behind as seen in figure 1.4. 10^{-5} to 1 second after the Big Bang, the axion begins to couple to QCD. This is when the temperature of the Universe drops to the confinement scale ($T \sim \Lambda_{\text{QCD}}$), when quarks become confined in hadrons such as protons and neutrons. When this happens, the angular shift symmetry will be broken, allowing the axion to develop a small mass and domain walls to appear in the Universe. Domain walls and strings are topological defects which store much of the energy density of the ψ field. Their dynamics are complicated and can only be studied numerically. Thus, providing the impetus for our project to simulate their dynamics.

Interestingly, quasi stable objects called oscillons occur naturally as solutions to a non-linear equation of motion during a brief period of axion mass growth. These results are unexpected but have surprising ramifications. The non-linear evolution of the axion field in the early Universe will cause large amplitude density fluctuations [64], leading to very dense axion clumps or tiny gravitationally bound miniclusters [44, 65]. Thus, if axions were to be dark matter, halos of galaxies would be expected to be clumpy and inhomogeneous rather than have a smooth, uniform distribution.

This thesis will aim to study the complicated dynamics of axions in the early Universe and simulate the case where the $U(1)_{\text{PQ}}$ symmetry of the complex scalar ψ is spontaneously broken after inflation. We will study the Physics of the topological defects such as strings and domain walls which are non-trivial field configurations which can only be simulated numerically. Later, we will examine the oscillons, which are quasi stable objects which appear at the locations of collapsed strings during a short time after QCD phase transition. These are important as they will lead to energy overdensities in the Universe which will cause the inhomogeneities in the mass distribution of the Milky Way galaxy.

Chapter 2 will explain how the simulations were setup, chapter 3 will explore the results of the simulations and chapter 4 will discuss the physical implications of those results and how to detect the axion.

Chapter 2

Simulation Setup

2.1 Broken Before Inflation

We now look at the case where PQ symmetry breaking in figure 1.2 occurs before or during inflation. Inflation causes small initial perturbations to blow up beyond the horizon, effectively homogenising all quantum fields to an observer. If $f_a > T_I$ where T_I is the temperature when inflation occurs, PQ symmetry is broken before inflation. This causes ψ to roll down the potential to its new VEV with an angular freedom which is the axion $a = \theta f_a$. After symmetry breaking, there are causally disconnected patches with different field values of $a(x, t)$ such that θ_i from figure 1.1 is different for each patch. Being causally connected, rapid expansion stretches out each θ_i so that the θ_i of our Hubble volume has a single uniform θ_i . The initial value of $\theta_i \in (-\pi, \pi]$ is therefore completely random given that there is no initial ‘tilt’ in the ‘Mexican Hat potential’ which favours one θ_i value over another.

Thus, we only have two parameters in this scenario. The axion mass m_a and the initial θ_i [17]. The evolution of the axion field will be determined by a simple wave equation. Eventually, the QCD phase transition will occur and the entire field will move towards $\theta = 0$ to solve the strong CP problem. The Hubble friction acts as a damping term and there will be some oscillation about $\theta = 0$ until finally settling to $\theta \leq 10^{-10}$ when $t = t_{cold}$. t_{cold} describes a time scale longer than the axion de Broglie wavelength which is dependent on the zero-temperature axion mass.

Thus, if we want the axion to fulfill all or a proportion of dark matter, then for a given initial θ_i , f_a must be adjusted in order to generate the desired dark matter abundance.

2.2 Broken After Inflation

If PQ symmetry is broken after inflation $f_a < T_I$, the axion field is not homogeneous. Each point in the field initially takes on a random $\theta_i \in (-\pi, \pi]$ and evolves from this starting point. Computing the abundance of dark matter becomes difficult as relics of the PQ phase transition remain in the form of axion strings. Strings complicate cosmology as they enter a ‘scaling solution’. Strings follow a kind of self-organised criticality [32]. This means as the universe expands, the number of strings per Hubble volume also increases until the string density crosses a point whereby the configuration is unstable. When this occurs, strings will seemingly correct themselves by cutting themselves into loops, recombining and decaying by emitting axions to maintain the scaling solution. Later on during the QCD phase transition, domain walls also appear and complicate field dynamics further, making it difficult to find an axion mass which produces an abundance of dark matter which is consistent with observations of our Universe. These complications make it necessary to use numerical simulations to determine the axion mass.

2.3 Setup

We will now describe how we setup a numerical simulation to evolve the axion field through the early Universe.

The simulation was written in Julia to take advantage of its just-in-time compilation and multithreading capabilities. Our goal was to study how the axion field evolved throughout the early Universe. The algorithm

involved starting with an initial $N \times N$ grid¹ and using an equation of motion (EOM) to calculate the grid values at the next time step using the Leapfrog Algorithm.

We perform numerical simulations of a complex scalar PQ field $\psi = re^{ia/f_a}$ whose angular mode describes the axion field and analyse how it evolves if PQ symmetry is broken after inflation has already occurred. Our theory which describes both the spontaneous $U(1)_{\text{PQ}}$ symmetry breaking and later the coupling to QCD is given by the following Lagrangian density

$$\mathcal{L} = \frac{1}{2}|\partial\psi|^2 - V(\psi). \quad (2.1)$$

The full potential is

$$V(\psi) = \frac{1}{2}m_h^2|\psi|^2 + \frac{\lambda}{4}(|\psi|^2 - f_a^2)^2 + m_a(T)^2f_a^2[1 - \cos \text{Arg}(\psi)], \quad (2.2)$$

where ψ is a complex scalar, T is the temperature, λ is a measure of the curvature of the ‘Mexican hat potential’, f_a is the axion decay constant, and $m_a(T)$ is the temperature dependent axion mass.

To model the evolution of the axion field, spacetime coordinates must be used. Rather than using flat Minkowski spacetime, the expanding universe requires the FLRW metric. Thus, the simulated grid will be in comoving coordinates such that the length of the grid $L \propto R(t)$, where $R(t)$ is the scale factor.

This means that the spacing between each lattice point also gets stretched as the simulation develops. Strings are associated with regions where $|\psi| < f_a$. The radius of string cores $\delta \sim m_r^{-1}$ do not increase with time and are determined by the mass of the radial mode m_r [33]. As we are simulating an effective axion model, λ and the axion mass m_a are used as free parameters. The grid is in comoving coordinates, causing the string core to shrink in the simulation and be represented as a smaller amount of lattice points in the grid over time. However, there is a finite amount of grid points. This causes a problem when the strings artificially disappear. As a result, the simulation has a time limit where anything past this time the simulation is no longer physical. To solve this, we use the fat strings trick [57] which is an unphysical method of keeping the number of lattice points per string length constant. However, when compared to physical simulations, it has been shown to not sizeably impact the dynamics or final results [32]. $m_r(t) = m_i\sqrt{t_i/t}$ is made to change with time such that the string radius does not vary in comoving coordinates, following $\delta(t) \sim t^{1/2}$ and allowing for a longer maximum simulation time. λ in equation 2.2 can be interpreted as the squared mass of the radial mode. By having m_r decrease in time, our simulations could be interpreted as modelling an axion theory where λ decreases, changing the shape of the Mexican Hat potential over time.

Due to this, the grid sizes required for a fat string simulation can be smaller as the string dynamics can be followed for a longer period of time. While this is not ideal, the results from the fat strings trick make it easier to clarify string dynamics [32]. This will lead to different quantitative results, though qualitative results will likely remain the same. However, this is not guaranteed.

To examine and study anything physical relating to our Universe, a simulation must be done in 3 spatial dimensions and without the fat strings trick. Simulating in 3D drastically increases computation times and to resolve the strings without the fat strings trick requires even more lattice points, further increasing computational demand. A method that allows the simulation of a physical Universe whilst saving computational time may be to use an adaptive mesh [15]. By increasing the spatial resolution in the regions where the string core is present, the dynamics of the field and strings can be followed for longer simulation times. Thus, leading to better quantitative results for a physical string network. We strictly study 2D simulations using the fat strings trick to reduce the computational time and attain qualitative results.

This finite grid also poses an issue when we consider how the axion field at the boundaries of the grid will evolve. Every point in the field is dependent on the dynamics of the rest of the field that it is in causal contact with, according to the equation of motion. We solve this problem by imposing periodic boundary conditions such that boundary lattice points can evolve in accordance with the rest of the grid. This puts a limit on the absolute time scale of the simulation. This is because a lattice point will affect its neighbouring lattice points. This perturbation will be carried on by those neighbours and due to the periodic boundary conditions imposed, the original lattice point will eventually experience own effect and the simulation will become unstable. This time limit is known as the light crossing time which is $t_f = 1/2N\Delta x/\Delta t$. N is the number of lattice points

¹Although the Universe is 3D, 2D simulations are used because 3D simulations are computationally demanding. However, all relevant physics can be captured in 2D simulations. The simulation code can be readily extended to 3D.

per side of the grid, Δx is the spacing between lattice points and Δt determines the temporal resolution of the simulation. We have avoided this time limit in our simulations.

2.4 Equations of Motion

The first term in the potential 2.2 $1/2m_{th}^2|\psi|^2$ accounts for thermal effects in the ψ field. $m_{th} = \lambda T^2/3$ and so, if we account for the look at the quadratic terms of $|\psi|$, we can see that the effective mass of ψ is

$$m_\psi^2 = \lambda \left(-f_a^2 + \frac{T^2}{3} \right). \quad (2.3)$$

Notice that when the temperature drops such that $T \lesssim f_a$, m_ψ^2 becomes negative. This reflects the breaking of $U(1)_{\text{PQ}}$ symmetry and the morphing of the potential into the ‘Mexican hat’ shape.

We can use the Lagrangian density from equation 2.1 and use the Euler Lagrange equations to find an EOM. Decomposing our complex scalar $\psi = \phi_1 + i\phi_2$ and assuming a radiation-dominated cosmological background in a flat expanding FLRW universe ($R(t) \sim t^{1/2}$), our EOMs become

$$\ddot{\phi}_1 + 3H\dot{\phi}_1 - \frac{1}{R^2}\nabla^2\phi_1 + \frac{1}{3}\lambda\phi_1 \left[3(\phi_1^2 + \phi_2^2 - f_a^2) + T^2 \right] - \frac{m_a(T)^2\phi_2^2}{(\phi_1^2 + \phi_2^2)^{\frac{3}{2}}} = 0, \quad (2.4)$$

$$\ddot{\phi}_2 + 3H\dot{\phi}_2 - \frac{1}{R^2}\nabla^2\phi_2 + \frac{1}{3}\lambda\phi_2 \left[3(\phi_1^2 + \phi_2^2 - f_a^2) + T^2 \right] + \frac{m_a(T)^2\phi_1\phi_2}{(\phi_1^2 + \phi_2^2)^{\frac{3}{2}}} = 0, \quad (2.5)$$

where R is the scale factor.

For simplicity, the EOM can be redefined following Buschmann et al. [16] with a dimensionless conformal time $\hat{\eta}$ such that

$$\hat{\eta} = \frac{R}{R(T = T_1)} = \left(\frac{t}{t_1} \right)^{\frac{1}{2}}, \quad (2.6)$$

where the time t_1 is when $T(t_1) \equiv T_1$. T_1 is a temperature defined differently in the PQ or QCD epoch in order to simplify our EOMs further later on. In our axion model, the mass of the axion grows until a cutoff temperature T_c which is when the axion reaches its zero-temperature value. The corresponding time when this occurs will be given by $\hat{\eta}_c = R(T = T_c)/R_1$. This allows us to rewrite equations 2.4 and 2.5 as

$$\psi_1'' + \frac{2}{\hat{\eta}}\psi_1' - \bar{\nabla}^2\psi_1 + \frac{1}{H_1^2} \left[\lambda\psi_1 \left(\hat{\eta}^2 f_a^2 (\psi_1^2 + \psi_2^2 - 1) + \frac{T_1^2}{3} \right) - m_a^2(T_1)\hat{\eta}^2 \frac{\min(\hat{\eta}, \hat{\eta}_c)^n \psi_2^2}{(\psi_1^2 + \psi_2^2)^{\frac{3}{2}}} \right] = 0, \quad (2.7)$$

$$\psi_2'' + \frac{2}{\hat{\eta}}\psi_2' - \bar{\nabla}^2\psi_2 + \frac{1}{H_1^2} \left[\lambda\psi_2 \left(\hat{\eta}^2 f_a^2 (\psi_1^2 + \psi_2^2 - 1) + \frac{T_1^2}{3} \right) + m_a^2(T_1)\hat{\eta}^2 \frac{\min(\hat{\eta}, \hat{\eta}_c)^n \psi_1 \psi_2}{(\psi_1^2 + \psi_2^2)^{\frac{3}{2}}} \right] = 0, \quad (2.8)$$

where $\phi_i = f_a\psi_i$ and $\phi'_i = \frac{d\psi_i}{d\hat{\eta}}$. The spatial gradient is $\bar{x} = a_1 H_1 x$. EOMs have now been written in terms of conformal time and dimensionless coordinates.

It is important to note that η_c is being used as an analog for the zero-temperature axion mass. $m_a^2(T_1)\min(\hat{\eta}, \hat{\eta}_c)^n$ grows until a cutoff time, capturing how the axion mass will grow until a cutoff temperature as seen in equation 1.3. Thus, our free parameter of the axion mass is now characterised by the critical time $\hat{\eta}_c$. We choose $\hat{\eta}_c = 2.8, 3.6$, and 6.0 when running our simulations. For a $\hat{\eta}_c = 0$ simulation which we view later on, this is equivalent to a scenario where the axion does not couple to QCD and remains massless.

2.5 PQ Epoch

For the PQ epoch, there is no coupling to QCD. Thus, we denote the conformal time in this epoch as $\tilde{\eta}$ and reserve $\hat{\eta}$ for the QCD epoch, where $\hat{\eta}_c$ is the cutoff time for the axion mass. We have chosen our initial starting time and grid side-length $L_{\text{PQ}} = 8000$ and conformal time units to match Buschmann et al. [16] as they perform simulations in 3D. This allows us in future to readily compare results for 3D simulations.

The starting point $\tilde{\eta}_i = 0.001$ is chosen. The simulation then proceeds with the initial time-step $\delta\tilde{\eta}_i = 0.004$ until $\tilde{\eta} = 250$, after which a variable time-step $\Delta\tilde{\eta}_i(250/\tilde{\eta})$ is used to maintain temporal resolution for stability. The simulation was stopped at a point in time $\tilde{\eta}_f$ when the oscillations in the radial mode of ψ are highly damped. The length of the grid L_{PQ} is chosen arbitrarily as to choose the speed at which the simulation dynamics will evolve. This is permitted as the length of the grid does not physically represent a distance. Choosing a smaller L_{PQ} will mean that the lattice spacing Δx will be smaller, allowing string dynamics to evolve through the PQ epoch much faster.

We begin our simulations of the PQ epoch with initial field conditions where PQ symmetry is extremely close to breaking. When this occurs less than a second after the Big Bang, temperatures are very high $T \gg \Lambda_{\text{QCD}}$, where $\Lambda_{\text{QCD}} = 400$ MeV is the confinement scale where QCD effects become relevant. Due to this, we can effectively set $m_a(T) = 0$ and there is no coupling of the axion to QCD during this epoch. Therefore our EOMs from equation 2.7 and 2.8 become

$$\psi_1'' + \frac{2}{\tilde{\eta}} \psi_1' - \bar{\nabla}^2 \psi_1 + \lambda \psi_1 \left[\tilde{\eta}^2 (\psi_1^2 + \psi_2^2 - 1) + \frac{T_1^2}{3f_a^2} \right] = 0, \quad (2.9)$$

$$\psi_2'' + \frac{2}{\tilde{\eta}} \psi_2' - \bar{\nabla}^2 \psi_2 + \lambda \psi_2 \left[\tilde{\eta}^2 (\psi_1^2 + \psi_2^2 - 1) + \frac{T_1^2}{3f_a^2} \right] = 0, \quad (2.10)$$

where $\tilde{\eta} = 1$ is fixed to be the time when $H_1 = f_a$.

To evolve the grids based on the EOMs from equations 2.9 and 2.10 it was necessary to calculate the spatial derivatives of a given field ψ

$$\nabla^2 \psi_{i,j} = \frac{-\psi_{i-2,j} + 16\psi_{i-1,j} - 30\psi_{i,j} + 16\psi_{i+1,j} - \psi_{i+2,j} - \psi_{i,j-2} + 16\psi_{i,j-1} - 30\psi_{i,j} + 16\psi_{i,j+1} - \psi_{i,j+2}}{12\Delta x^2}. \quad (2.11)$$

For the PQ epoch λ was taken to be 1. The ratio $(T_1/f_a)^2$ is given by [16]

$$\left(\frac{T_1}{f_a} \right)^2 \approx 8.4 \times 10^5 \left(\frac{10^{12} \text{ GeV}}{f_a} \right). \quad (2.12)$$

Thus, a grid of lattice points is setup with ψ_1 and ψ_2 fields representing the complex scalar. Each lattice point will be given a random $\theta_{\text{PQ}} \in (-\pi, \pi]$ and radial component $r = \sqrt{\psi_1^2 + \psi_2^2}$ which is very close to zero such that PQ symmetry is initially present. This done by randomly selecting values centred around 0 for lattice points of the ψ fields such that a thermal distribution is resembled. The velocities or ψ_1' and ψ_2' are initially 0 so no particular angle is favoured at the beginning of the simulation.

2.6 QCD Epoch

The final state of the PQ epoch is used as the initial state of the QCD simulation. The physical length of the grid L_{QCD} can be different from L_{PQ} depending on what physical length units are convenient. However, the ratio $L_{\text{PQ}}/\tilde{\eta}_f = L_{\text{QCD}}/\hat{\eta}_i$ must be maintained to preserve the status of the modes. Currently our simulations are showing some instability from the remaining strings of the PQ epoch during the change in epochs. We start the QCD epoch at the time $\hat{\eta}_i = 0.4$. The EOMs are evolved with the time step $\Delta\hat{\eta}_i = 0.001$. After $\hat{\eta} = 3$, an adaptive time-step $\Delta\hat{\eta}_i(3/\hat{\eta})^{3.34}$ is used.

During the QCD epoch $T \sim \Lambda_{\text{QCD}}$ and so the axion mass term from equations 2.7 and 2.8 is non-negligible. We define $\hat{\eta} = 1$ to be the time when $H_1 = m_a(T_1)$. Physically, this represents the time when the axion starts to roll down to the new minimum of the potential where $\theta = 0$. The axion field begins to oscillate shortly after when $m_a(t) = 3H(t)$. The EOMs in equations 2.7 and 2.8 become

$$\psi_1'' + \frac{2}{\hat{\eta}} \psi_1' - \bar{\nabla}^2 \psi_1 + \tilde{\lambda} \hat{\eta}^2 \psi_1 (\psi_1^2 + \psi_2^2 - 1) - \hat{\eta}^2 \min(\hat{\eta}, \hat{\eta}_c)^n \left(\frac{\psi_2^2}{(\psi_1^2 + \psi_2^2)^{\frac{3}{2}}} \right) = 0, \quad (2.13)$$

$$\psi_2'' + \frac{2}{\hat{\eta}} \psi_2' - \bar{\nabla}^2 \psi_2 + \tilde{\lambda} \hat{\eta}^2 \psi_2 (\psi_1^2 + \psi_2^2 - 1) + \hat{\eta}^2 \min(\hat{\eta}, \hat{\eta}_c)^n \left(\frac{\psi_1 \psi_2}{(\psi_1^2 + \psi_2^2)^{\frac{3}{2}}} \right) = 0, \quad (2.14)$$

where the T_1 contribution has been neglected as it is small compared to f_a . The parameter $\tilde{\lambda}$ is defined by

$$\tilde{\lambda} = \lambda \left(\frac{f_a}{m_a(T_1)} \right)^2. \quad (2.15)$$

λ is the square of the radial mode. It can be interpreted as a parameter for the curvature of the axion potential in the radial direction. Through our simulations we can see identify what effect changing the shape of the potential has on our results. We choose λ in the ranges of 1024 and 5504 arbitrarily.

When the topological defects or string network has completely collapsed in this epoch, shortly after, we switch to axion-only EOMs for computational efficiency. This is because the entire field will mostly be contained, with small fluctuations, about the minimum at $\theta = 0$. When we switch to this EOM, we no longer track the saxion field. Doing this is fine as we do not expect any additional energy contributions to the saxion field at this point in the simulation. Our axion is defined by $a = f_a \tan^{-1}(\phi_2/\phi_1)$ and has the Lagrangian

$$\mathcal{L} = \frac{1}{2} (\partial a)^2 - m_a^2(T) f_a^2 \left[1 - \cos \left(\frac{a}{f_a} \right) \right]. \quad (2.16)$$

The EOM calculated from the Lagrangian in equation 2.16 is

$$\theta'' + \frac{2}{\hat{\eta}} \theta' - \bar{\nabla}^2 \theta + \hat{\eta}^2 \min(\hat{\eta}, \hat{\eta}_c)^n \sin(\theta) = 0, \quad (2.17)$$

where $\theta = a/f_a$.

During the QCD epoch, the size of the grid poses a computational problem. This is because the simulation is attempting to simulate the entire evolution of the axion field within a reasonable time frame. The exponent $n = 6.68$ may cause excessive tilting of the potential leading to an unphysical destruction of the string network. If this occurs, the QCD potential has tilted so much that the saxion no longer has a local minimum at $\theta = \pi$. This means that in figure 1.5, the point at $\theta = \pi$ is no longer a saddle point. Thus, rather than moving down the potential using the angular freedoms, the tilt of the potential may allow the roll-over-the-top mechanism whereby the axion field will roll unimpeded over the top of the ‘Mexican hat potential’ to reach the $\theta = 0$ minimum [65]. Therefore, the value of n must be chosen appropriately. Someone simulating a 8192^2 grid may choose $n = 6.68$ whilst for a 512^2 grid, $n = 1$ may be chosen to avoid unphysical effects that can only happen within a simulation. Despite these unphysical effects, a $n = 6.68$ simulation with a smaller 512^2 grid is actually able to capture the relevant qualitative physics without expending too much computational resources. This simulation can later be performed again on larger grids without the fat strings trick if a quantitative result is to be obtained.

Chapter 3

Results

There is a lot of information that can be gleaned from these simulations. However, it is important to stress that these results are qualitative only. This is because we simulate 2D grids using the fat strings trick for computational efficiency. However, they still reveal important results about the energy distribution of the ψ field as a result of the axion theory. For our simulations, we have arbitrarily chosen $f_a = 10^{15} \text{ GeV}$ as it is in the estimated range for which one can obtain the correct dark matter density [16].

3.1 PQ Epoch

The PQ simulation begins directly before $U(1)_{\text{PQ}}$ symmetry breaking. Thus, initially the field values will take a random $\theta \in (-\pi, \pi]$ as to resemble a thermal distribution as seen in figure 3.1a. In addition, the modulus of the complex scalar ψ begins very close to 0. The field values of ψ will quickly fall to the new non-zero vacuum expectation value (VEV) such that the field will be allowed to settle so there is a smooth continuous angle change across the field with exceptions being at the string locations in figure 3.1b.

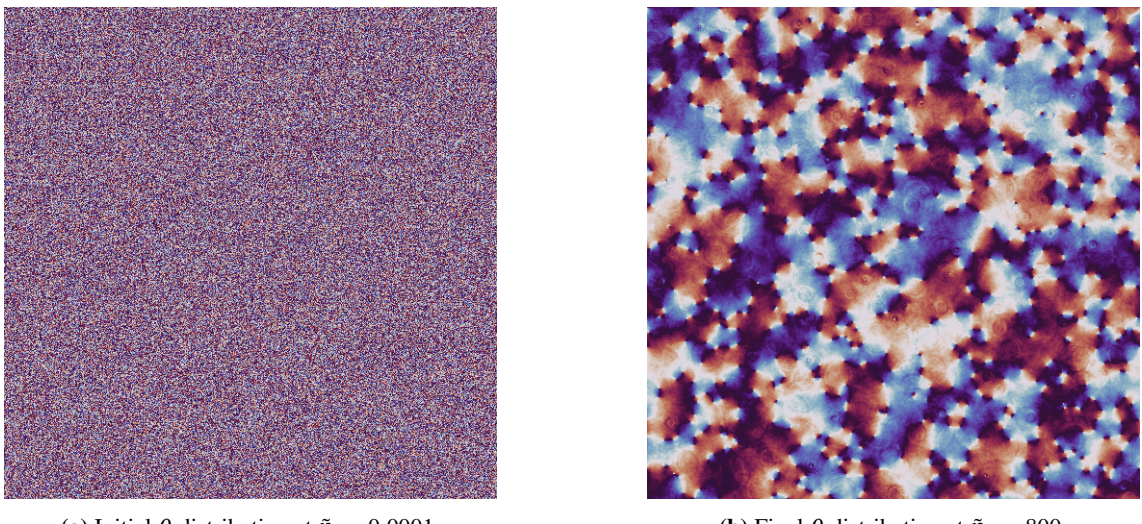


Figure 3.1: θ distribution for a 512×512 2D grid at the start and finish of the PQ epoch.

The string finding algorithm is based on the θ difference between 4 neighbouring lattice points from figure 1.3. Initially, the string finding algorithm counts around 30000 strings in the simulation. Keep in mind that this is a 512^2 grid simulation and thus, there are 262144 grid points. This means that the string finding algorithm classifies much of the field as a string. This makes sense, as in this simulation $T \gg \Lambda_{\text{QCD}}$ and temperatures are still very high. Thus, the field is highly energetic and the bulk of the field can easily reattain $U(1)_{\text{PQ}}$ symmetry and form strings. The definition of a string is not too well defined at the start of the simulation as most of the field has not yet settled into the new non-zero VEV of the ‘Mexican hat potential’.

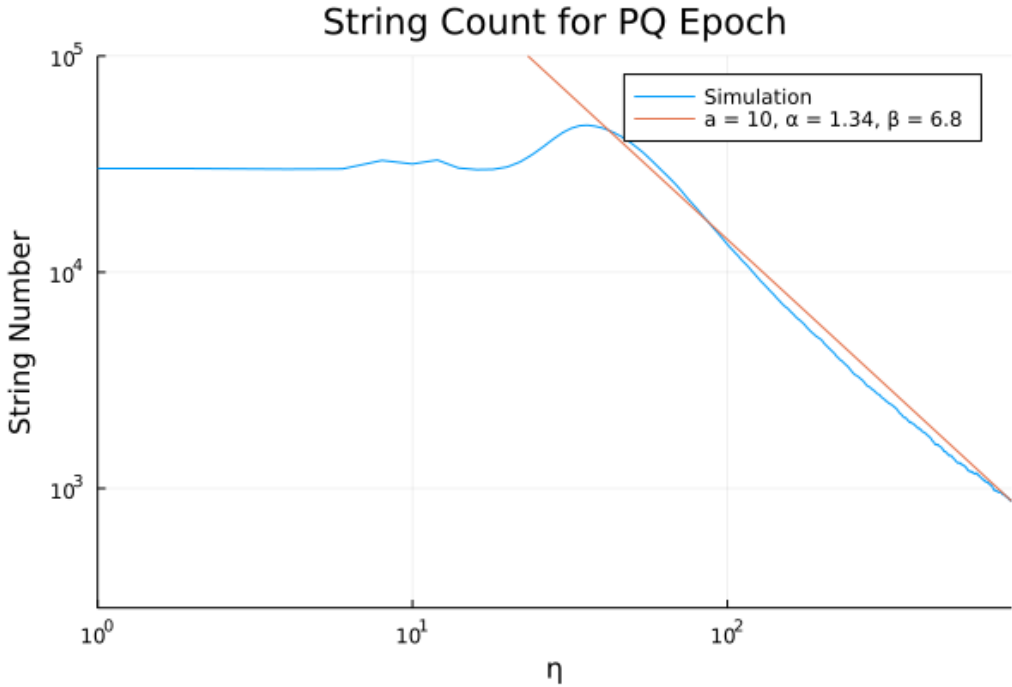


Figure 3.2: Initially, at high temperatures of the early Universe, the whole field is very energetic and thus the string finding algorithm has counted almost the entire field is in a string-like state. The number of strings over time in the PQ epoch linear for a log-log curve. The number of strings seems to follow a power law equation.

Only, once the field has mostly settled into the VEV, is the string finding algorithm able to correctly identify the number of strings in the simulation. When this happens, the string number decays linearly in a log-log plot. It seems to follow

$$\log_a \xi = -\alpha \log_a \eta + \beta \quad (3.1)$$

where α, β are just constants, a is an arbitrarily chosen exponent and ξ is the number of strings. This is a power law equation. For our PQ epoch simulation, we found that $\alpha \approx 1.34, \beta \approx 6.8$ for the exponent $a = 10$.

We can decompose the complex scalar into ψ_1 and ψ_2 fields, to find r as saxion field and a as the axion field as follows

$$r = \sqrt{\psi_1^2 + \psi_2^2}, \quad (3.2)$$

$$a = f_a \tan^{-1} \left(\frac{\psi_2}{\psi_1} \right). \quad (3.3)$$

Using these equations, we are able to obtain 2D arrays representing the saxion and axion field in our simulations. First, the FFTW.jl package in Julia was used to compute the Fourier transforms of these arrays. Next, the power spectrum was obtained by squaring the result of the Fourier transform. After this, the 2D power spectrum was flattened into one dimension and binned accordingly. Thus, allowing us to plot the power spectrum for the ‘wavelength’ of 1/256 to 1. This ‘wavelength’ is essentially a length scale related to half the number of lattice points for a side in the 512^2 grid. We use wavelength here as it more appropriately captures the ideas behind the analysis. For a short wavelength perturbation, this means that energy in the field is localised to smaller regions whilst for a long wavelength perturbation, that perturbation is spread across the field. For a classical field, a saxion is essentially a perturbation (fluctuation) in the radial mode whilst an axion is perturbation (fluctuation) about the angular mode of the potential.

For the PQ epoch in figure 3.3, the power spectrum tells us that a lot more energy is stored in short wavelength modes compared to long wavelength modes. This means that a lot of energy and fluctuations in the saxion field are localised to smaller areas. This makes sense as there are a lot of strings in the PQ simulation. Strings will collide over the course of the simulation, the field values at locations of collided strings are able to roll down the potential and fluctuate about the radial mode of the VEV.

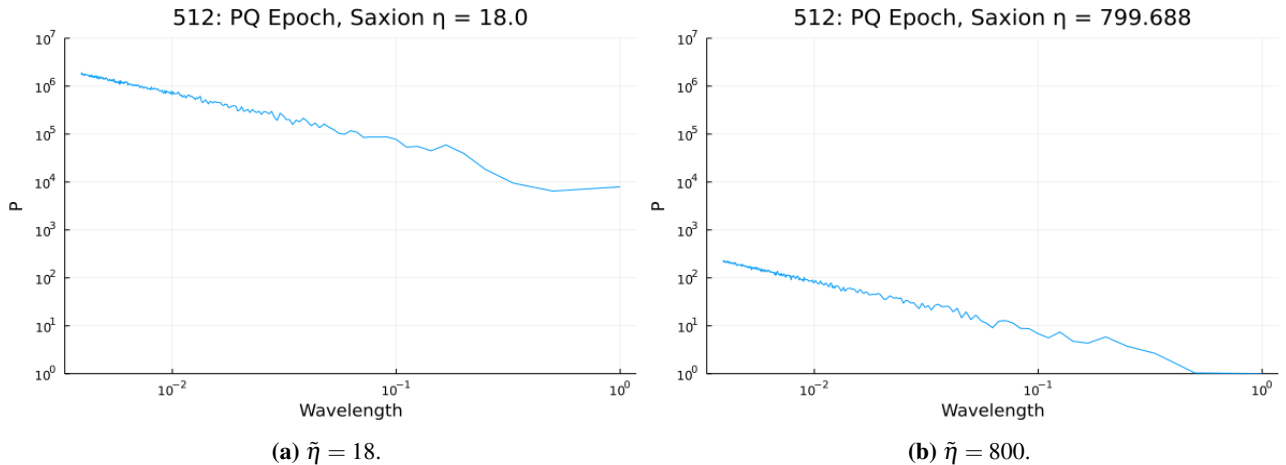


Figure 3.3: The power spectrum of the saxion field decreases over time. This because over time, the radial fluctuations of the field are allowed to settle about the non-zero VEV of the PQ epoch. Fluctuations of the saxion field are very small at $\tilde{\eta} = 800$ compared to earlier in the simulation.

Initially, when $\tilde{\eta} = 0.0001$, there is effectively no energy stored in the saxion field. This is because the initial conditions are such that the modulus is close to zero. By the time $\tilde{\eta} = 18$ in figure 3.3a arrives, much of the field has rolled to the non-zero VEV and has large fluctuations about the radial mode of the potential. The power spectrum of the saxion field reflects this. Over time, the saxion field becomes less energetic as seen in figure 3.3. This is due to an expanding and cooling temperature of the Universe where fluctuations in the radial mode are damped, allowing the field lattice points to settle in the VEV of the ‘Mexican Hat potential’.

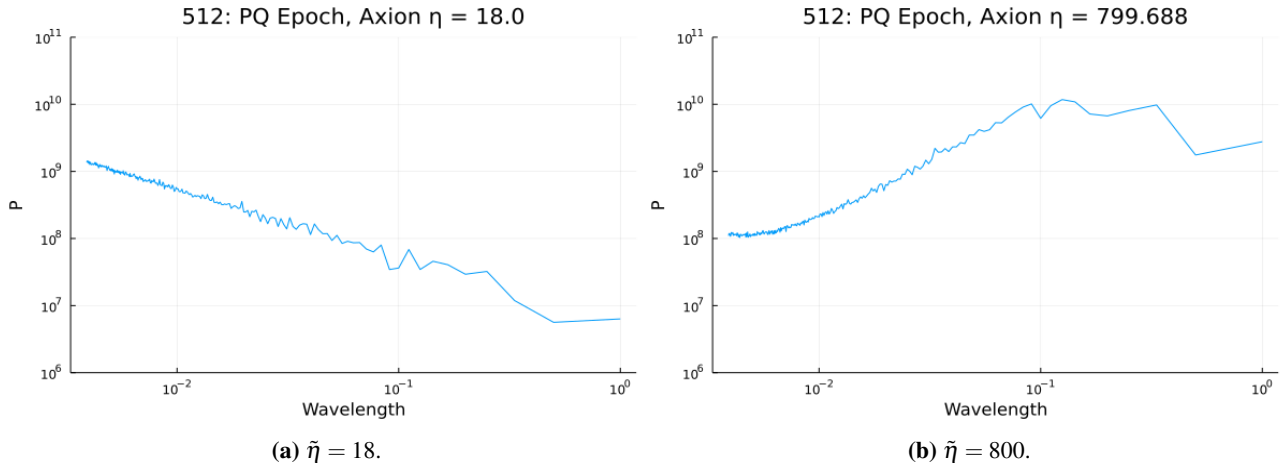


Figure 3.4: The power spectrum of the axion field increases over time as when the Universe cools, more regions of the field settle to the non-zero VEV which has an angular freedom. It can be observed that the energy stored in the shorter wavelength modes of the axion actually decrease over time, whilst the total energy in the longer wavelength modes increase.

Whilst the energy of the saxion field decreases in the simulation, the energy stored axion field increases over time as seen in figure 3.4. This is because as the temperature cools, the angular mode of ψ becomes relevant. The energy or amount of fluctuations in the axion field increases as the field begins to interact in an attempt to achieve a more stable field configuration.

In figure 3.4a there is more energy stored in smaller wavelength modes. This makes sense as early in the simulation, lots of energy in the axion field is localised in the numerous amounts of strings which have a small width. However, when strings collide, the energy stored in the strings will be released as axions spreading angular fluctuations across the field. This is why in figure 3.4b, the energy of the field has been moved to longer wavelengths modes as many of the early strings have collided.

3.2 QCD Epoch

The end of the PQ epoch in figure 3.1b is used as the initial conditions to start the QCD epoch. Because the end of the PQ epoch and start of QCD epoch is not completely contiguous as Δx between epochs are not the same. Thus, there will initially be some perturbations but the field will settle and behave regularly if given some time to settle. Thus, we plot the saxion and axion field at $\hat{\eta} = 0.8$ rather than at $\hat{\eta} = 0.4$, the supposed start of the simulation. All simulations have the use the same initial condition. There are three parameters we vary, they are λ , η_c and n .

There are a few parameters that are considered. First, is the λ term of the potential from equation 2.15. This could be used as a measure for the curvature of the Mexican Hat Potential in the radial direction. By increasing λ would increase the curvature of the potential. We have explored $\lambda = 1024, 1448, 3072, 3584, 5504$.

The second parameter is $\hat{\eta}_c$ is used as an analog for the zero-temperature axion mass. A larger $\hat{\eta}_c$ means that the axion mass grows to a larger value before stopping. We have explored $\eta_c = 2.8, 3.0, 3.2, 3.4, 3.6, 6.0$.

n is the power law index for the temperature dependence of the axion mass. Different axion models will have different values for n . A larger n means that the axion couples more strongly to QCD and that the axion mass grows at a faster rate.

Unless specified, the simulations for the power spectrum set $\lambda = 1024$, $\hat{\eta}_c = 2.8$ and $n = 1$.

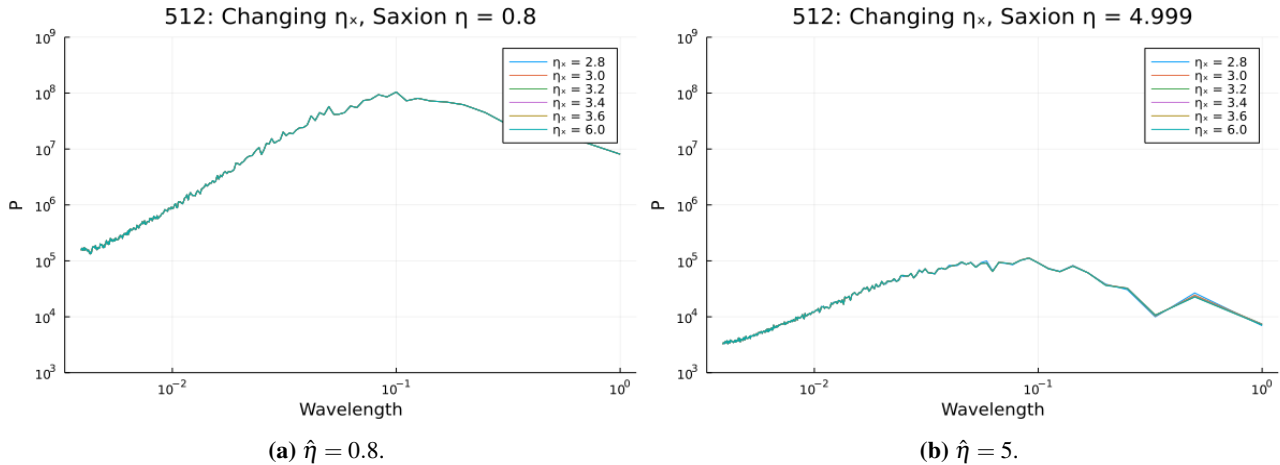


Figure 3.5: Changing the zero-temperature axion mass (η_c) does not affect the energy stored in the saxion field.

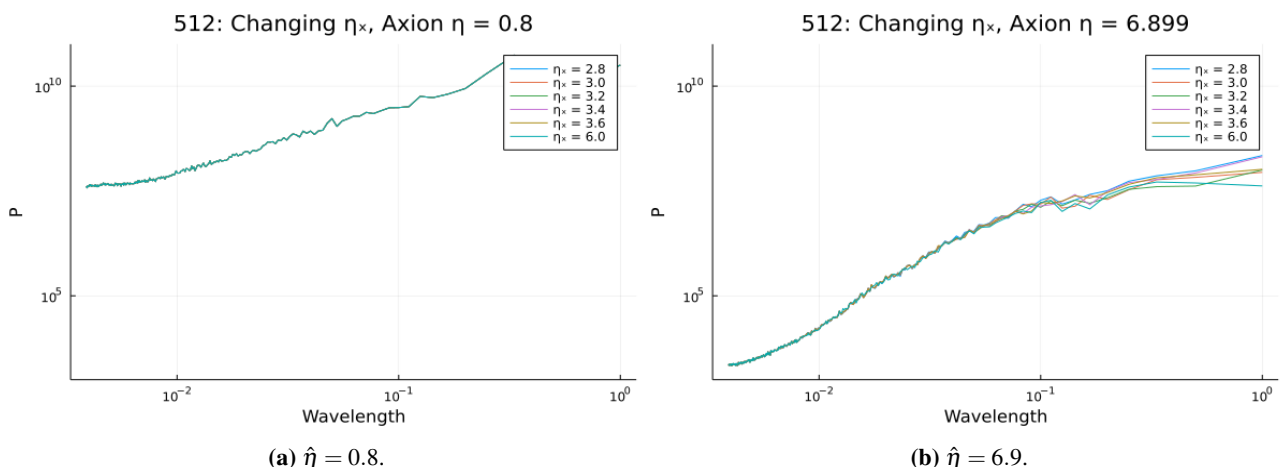


Figure 3.6: Changing the zero-temperature axion mass (η_c) does not seem to change much in the axion field. Perhaps the only difference can be seen in 3.6b where the longer wavelength modes of the axion field are more suppressed in the $\hat{\eta} = 6.0$ simulation.

Changing zero-temperature axion mass via the $\hat{\eta}_c$ parameter does not change the overall energy stored in the saxion and axion fields. This is because it requires time for the axion mass in simulations to grow until it reaches its zero-temperature mass. Therefore, these simulations are identical until $\hat{\eta} = 2.8$, which is the cutoff time for

axion mass growth for one of the QCD simulations. By this time, much of the field has already settled about the minimum about $\theta = \pi$. Thus, preventing any large scale deviations from appearing in the power spectrum. In figure 3.6b, it can be seen that the overall fluctuations of the field for the $\hat{\eta}_c = 6.0$ case is more suppressed. This is due to a stronger axion coupling to QCD in the $\hat{\eta}_c = 6.0$ simulation which damps angular fluctuations to a higher degree. We will discover later on, the zero-temperature axion mass does play an important role in how energy is distributed throughout the field.

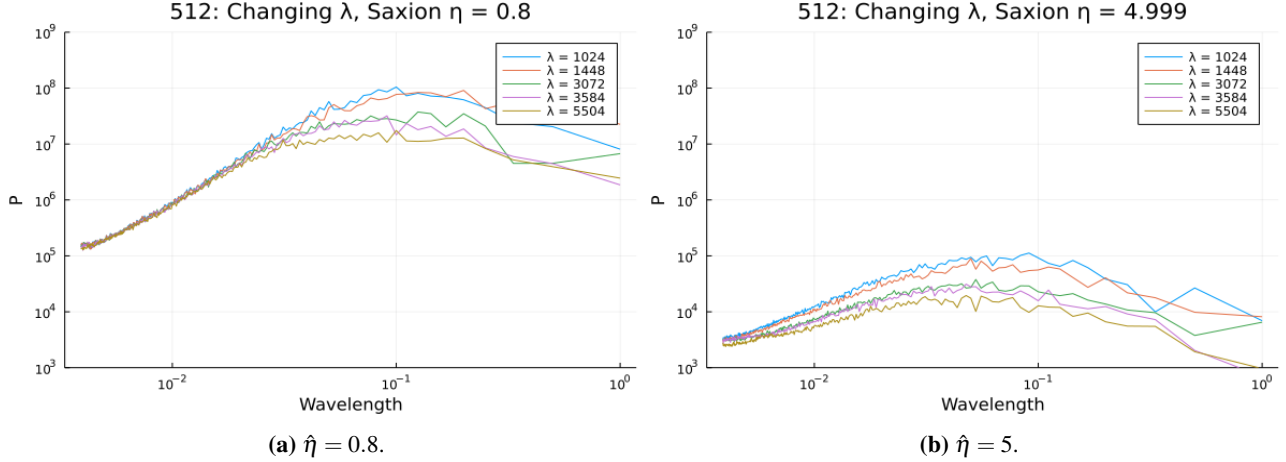


Figure 3.7: Changing λ seems to have a large effect on the saxion field power spectrum. The larger the λ is the larger energy stored in the saxion field.

A large λ would lead to a higher degree of curvature and steeper ‘Mexican hat potential’ in the radial mode. As our initial conditions are such that most of the field has already settled into the VEV, more energy is required to induce fluctuations in the radial mode, explaining figure 3.7. We can also see, that the short wavelength modes are unaffected by a change in λ . This is because strings are locations where $U(1)_{PQ}$ is restored. As a consequence, they do not have much fluctuations in the radial mode.

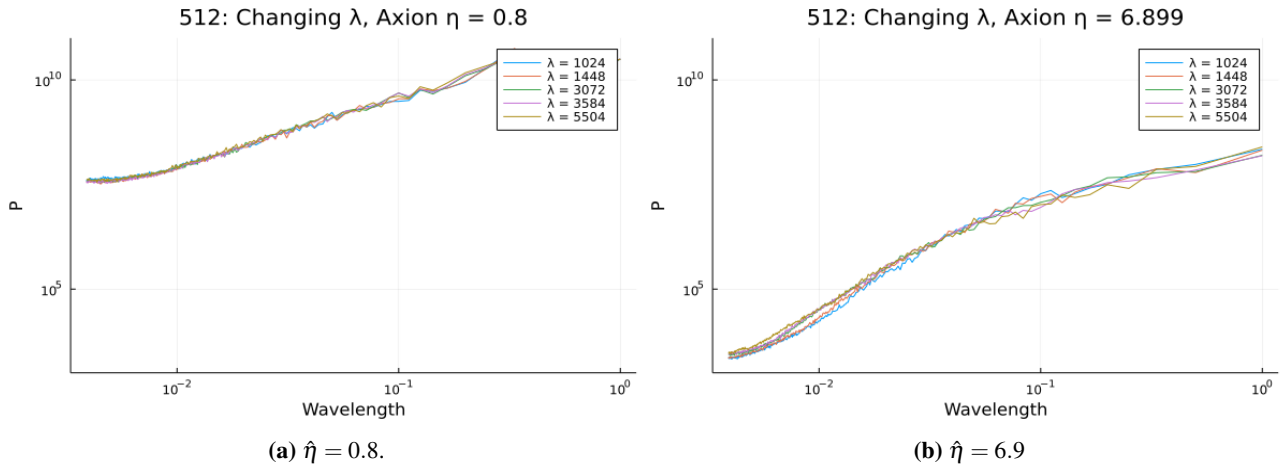


Figure 3.8: Changing λ does not seem to have much affect on the energy of the axion field.

λ seems to only effect the energy of the saxion field. This makes sense as λ is effectively a parameter describing the curvature of the potential in the radial direction. λ does not affect the angular shape of the potential and this is reflected in the power spectrum.

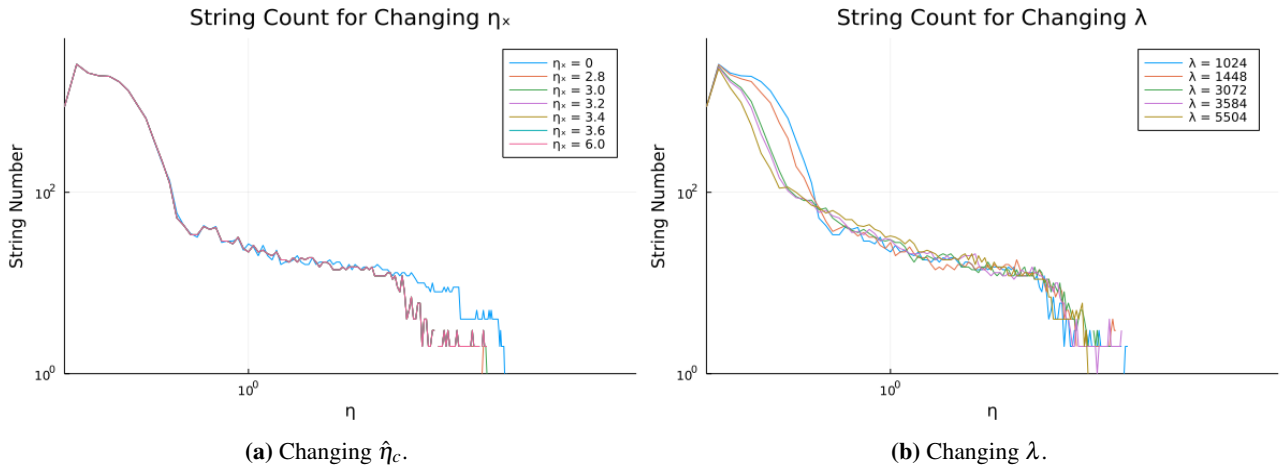


Figure 3.9: Changing $\hat{\eta}_c$ or λ does not have a big affect on the string count in the simulations. In the scenario where $\hat{\eta}_c = 0$, this is equivalent to a simulation where there the axion is massless. If we observe the curve for figure 3.9a, we see that the power law equation for string count is maintained in the $\hat{\eta}_c = 0$ simulation.

It seems as though changing η_c or λ does not seem to have much effect on the string number as seen in figure 3.9. It is important to note that for figures 3.9 and 3.10, the initial drop in string number is unphysical. This is due to the fact that the initial simulation is unstable when transitioning between PQ and QCD epochs. After the initial drop, string number follows the same power law equation. This is then followed by another drop in string number, this time due to a physical mechanism. As the axion mass increases, it seems to break the power law equation the the string count follows. This can be seen in figure 3.9a where if there is no coupling to QCD for the simulation where $\hat{\eta}_c = 0$, then the power law curve is maintained. This seems to suggest that the axion coupling to QCD changes the behaviour of strings which are pulled together by the surface tension on domain walls [65].

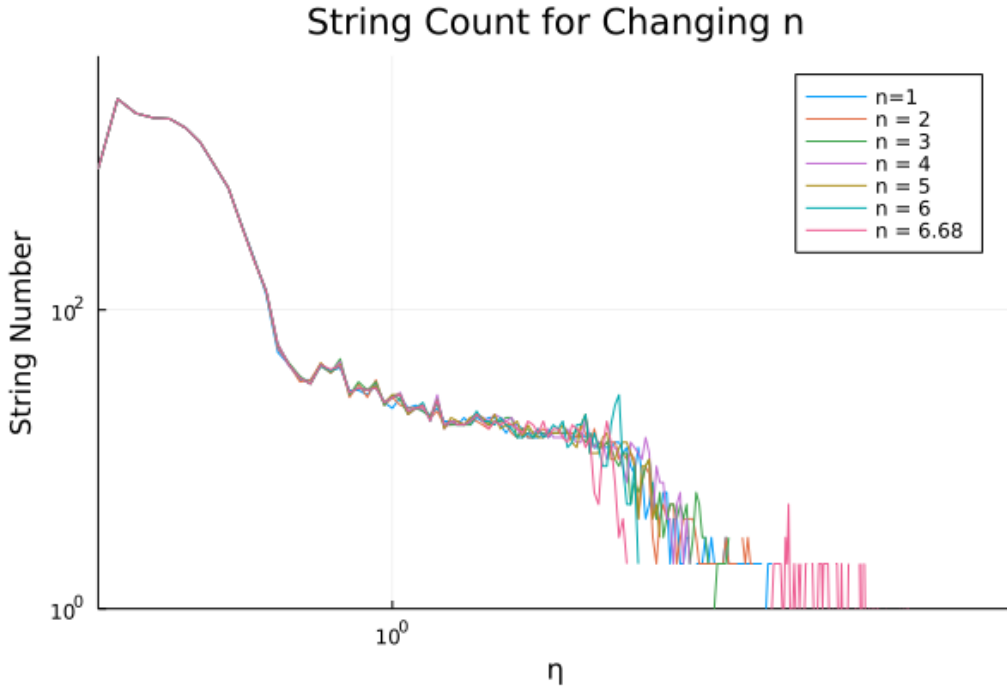


Figure 3.10: The larger the n , the faster the axion string network is destroyed. Observe that the pink curve for $n = 6.68$ is the first to reach a string count of 0, followed by the $n = 6$ curve.

It is important to note that in these simulations, the tilting of the potential gradually increases. This is why the power law pattern for string count is followed initially. However, as the tilting of the potential becomes greater, this power law curve for string count is not followed. The larger the n , the faster the axion mass grows and tilting of the potential. $n = 6.68$ is the strongest axion coupling to QCD, and thus, the tilt of the potential

is the greatest in this scenario. What we observe is that a stronger coupling to QCD accelerates the collapse of the axion string network.

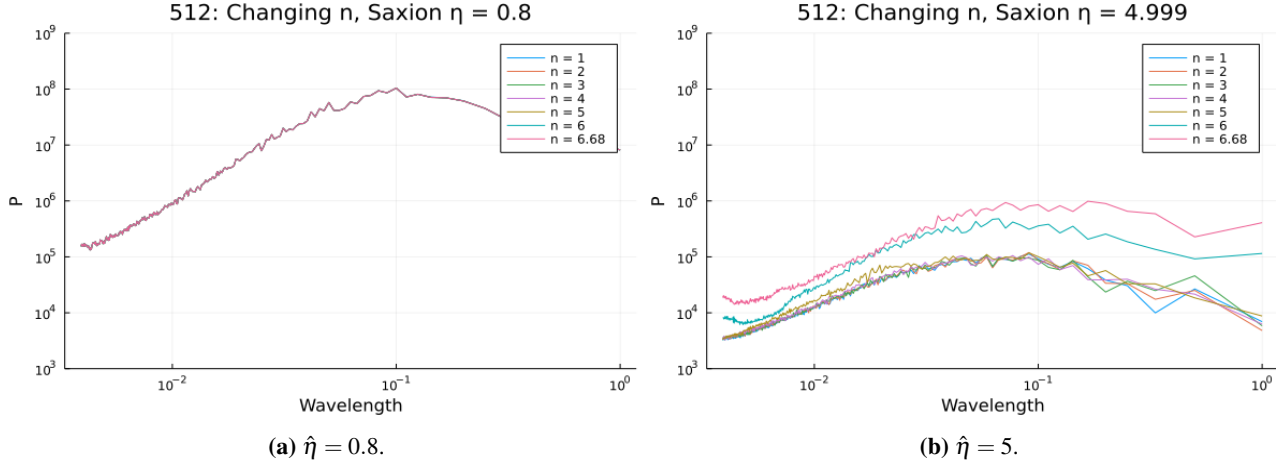


Figure 3.11: Changing n significantly changes the energy stored in the saxion field. A larger n means that the tilt of the potential is greater. This means that the amplitude of fluctuation in the radial mode when a field point rolls down the potential will be greater.

As seen in figure 3.11, a larger axion coupling to QCD leads to more fluctuations in the saxion field. n dictates zero temperature mass of the axion and also the rate of which the axion's coupling to QCD grows. When strings collide in the larger n simulations, their field values are met with a steeper potential to roll down to reach the minimum at $\theta = 0$. Thus, the amplitude of oscillations in the radial mode will be larger for the $n = 6.68$ case and this is reflected in the power spectrum in figure 3.11b.

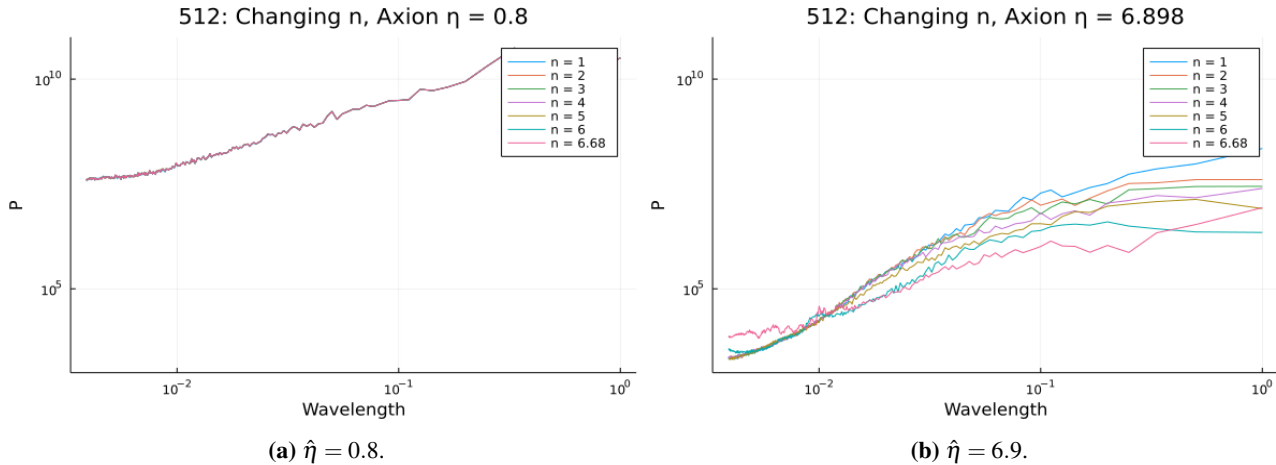


Figure 3.12: Changing n changes the energy in the axion field. At the end of the simulation, a larger n means less energy is stored in the axion field.

A larger coupling to QCD means that the angular potential of the field because much steeper, driving to $\theta = 0$. This means that the oscillating θ about $\theta = 0$ has a much smaller amplitude. As a result, the smaller energy in the axion field for larger n in figure 3.12b makes sense.

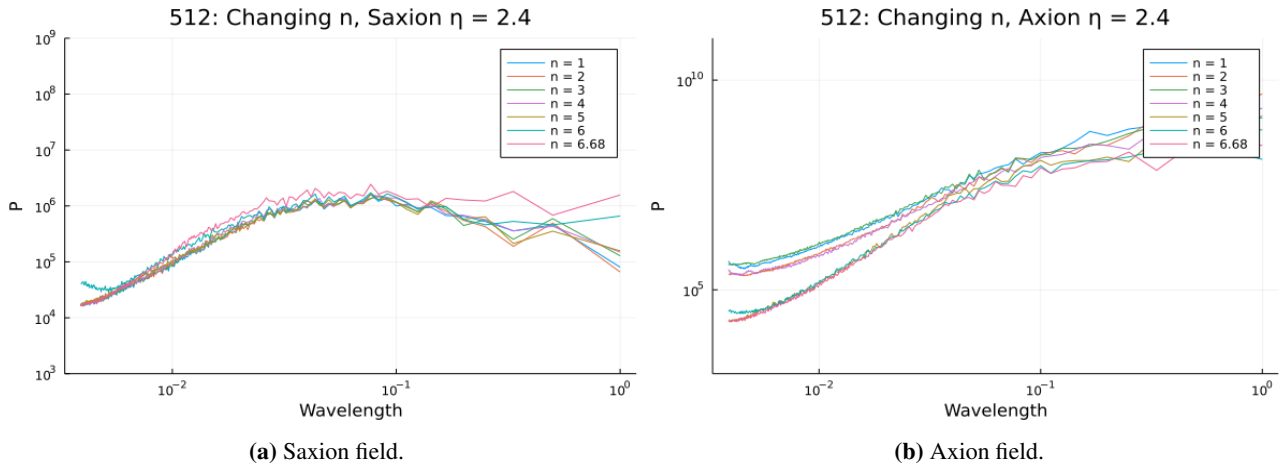


Figure 3.13: At $\hat{\eta} = 2.4$, $n = 1, 2, 3, 4$ still have strings in their simulations. The $n = 5, 6, 6.68$ simulations have no strings and less energy is stored in the axion field at the shorter wavelengths.

Figure 3.13 demonstrates that once the string network is destroyed, the energy previously stored in the strings converted into fluctuations about the VEV. The short wavelength energy contributions to the axion field energy are due to the axion string network. When $\hat{\eta} = 2.4$ the axion string network has not collapsed for the $n = 1$ case whilst it has already collapsed for the $n = 6.68$ scenario as seen in figure 3.14. This is reflected in figure 3.13b where for the shorter wavelengths, the curves for $n = 6.68$ and 6 are lower than the rest of the curves. In those simulations the axion string network has already been destroyed at $\hat{\eta} = 2.4$. However, if we observe figure 3.13a, we see there is a larger energy contribution in the saxion field for large n . This is because the field values previously at the string locations are allowed to roll down the potential and fluctuate around the radial mode VEV. Hence, from power spectrum plots, we can identify the time when the axion string network is destroyed as the energy stored in the axion field gets converted to the saxion field.

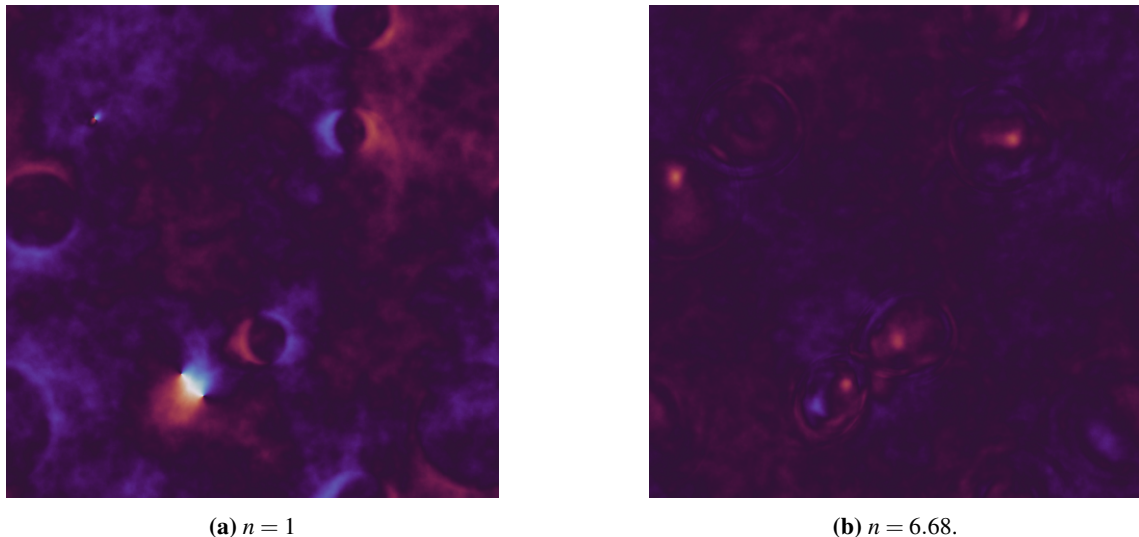


Figure 3.14: θ distribution when $\hat{\eta} = 2.4$. Strings can still be seen in the $n = 1$ case, whilst in the $n = 6.68$ case, the string network has already collapsed.

3.3 String Dynamics

The overall energy density ρ of the ψ field can be calculated by

$$\rho_t = \frac{1}{2}\psi_1^2 + \frac{1}{2}(\nabla\psi_1)^2 + \frac{1}{2}\psi_2^2 + \frac{1}{2}(\nabla\psi_2)^2 + V(\psi). \quad (3.4)$$

For our energy density plots, the potential $V(\psi)$ is excluded, so $\rho = \rho_t - V(\psi)$.

The energy density used in the plots is $\ln(\rho/\bar{\rho})$ where $\bar{\rho}$ is the average energy density of the field. Since this is a logarithmic scale, we notice in figure 3.15 that significant amount of the energy of the ψ field is stored in strings and domain walls.

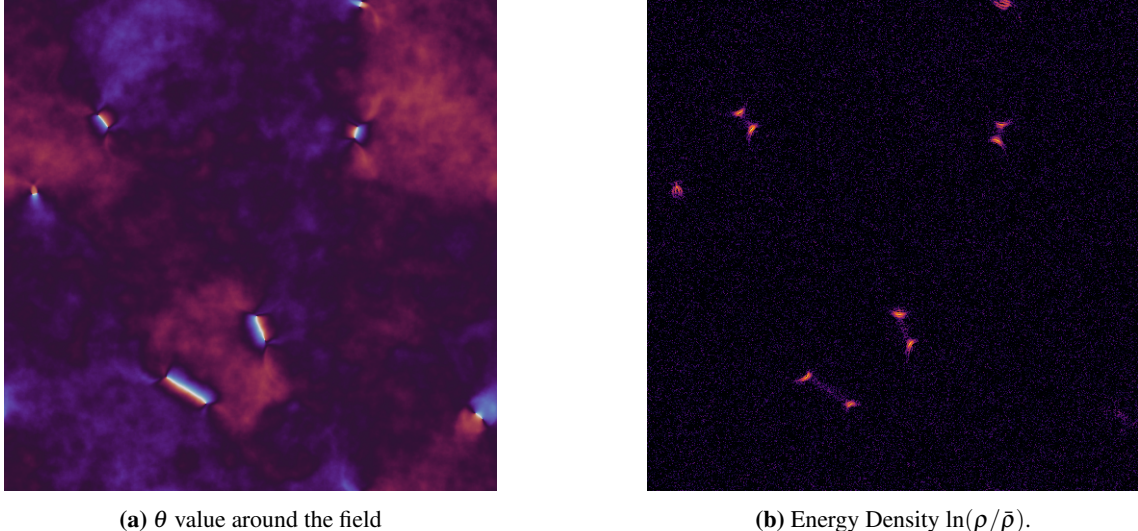


Figure 3.15: The strings and domain walls have a higher energy density than the rest of the field.

3.4 Opposite Chirality Strings

For these next string simulations, $\hat{\eta}_c = 0$ is chosen. Thus, the axion does not couple to QCD and the axion remains massless. Hence, domain walls do not appear in these simulations as there is no ‘tilt’ in the ‘Mexican hat potential’.

It is important to mention the concept of chirality. As seen in figure 3.16, the field can wind either clockwise or anti-clockwise about a string. We refer to strings with a different winding as opposite chirality strings.

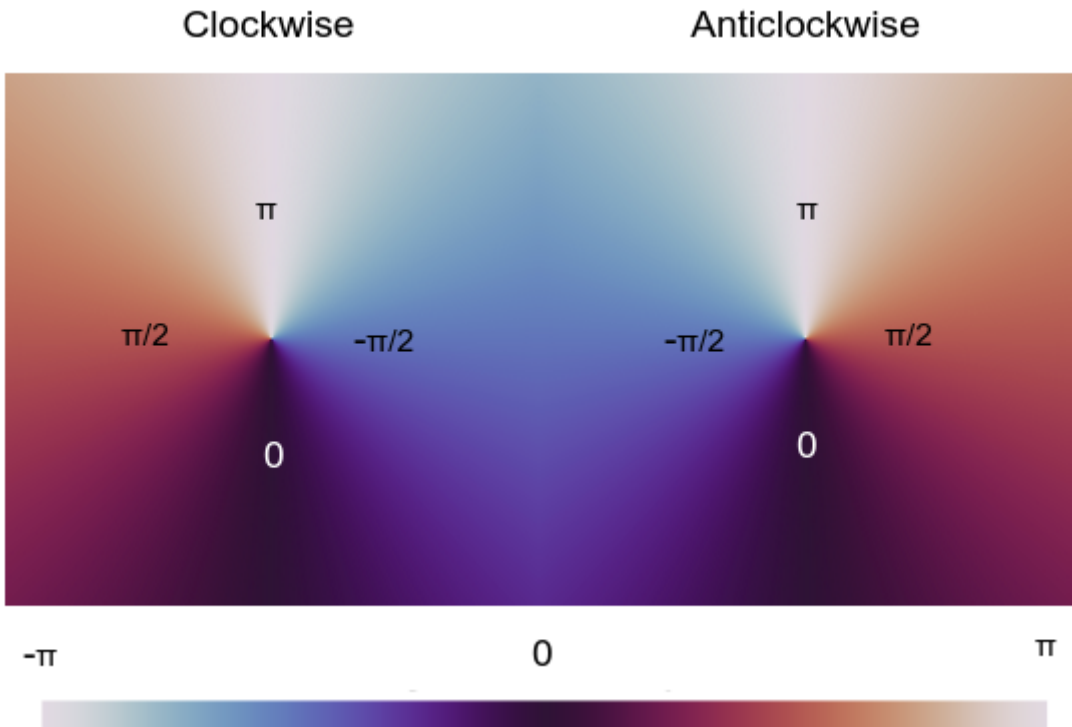


Figure 3.16: These are strings of opposite chirality. They wind about the $\theta \in (-\pi, \pi]$ in two different ways.

To test the dynamics of the string network, initial starting conditions were designed. The 4 strings case

is completely stable in a periodic grid. An image of this configuration can be seen in figure 3.17. This was achieved by constructing 4 grids, each with a single string, 2 clockwise and 2 anti-clockwise. These 4 grids were then merged together to construct a single grid.

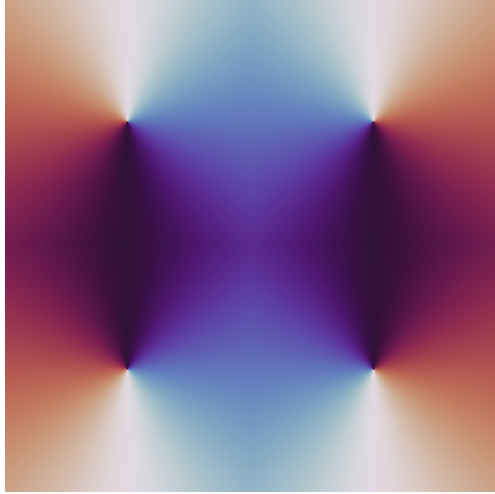
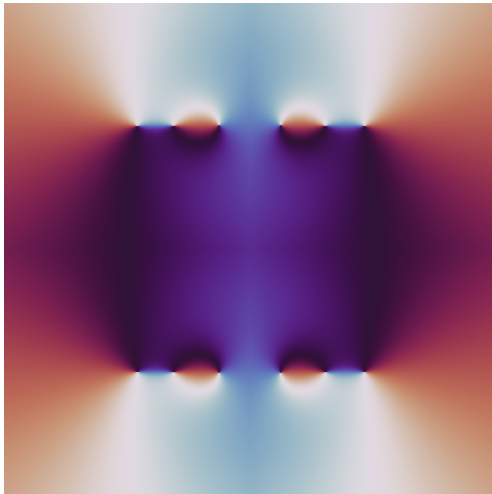


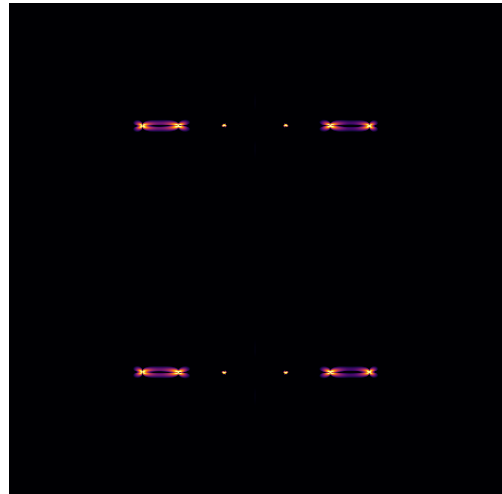
Figure 3.17: The manually inserted initial condition with 4 strings is completely stable

For these simulations we have also plotted the axion energy density. The energy density in strings is contained in their core and in the axion gradient field ∇a . This is because strings are associated with regions where $|\psi| < f_a$, and so the energy contribution due to fluctuations in the saxion field insignificant in comparison to their contribution to the axion field. Thus, we can obtain the energy density for relativistic axion modes ρ_a from the velocity field for the axion.

$$\rho_a = \frac{1}{2} \dot{a}^2 \quad (3.5)$$



(a) θ distribution around the field



(b) Axion energy density $\ln(\rho_a / \bar{\rho}_a)$.

Figure 3.18: Initial conditions have been changed to include 8 additional strings. On the right it can be seen that most of the energy in the axion field is stored in the strings.

Figure 3.18 emerged as a byproduct of requiring that there is a smooth angle distribution when the 4 string grids are merged together. If we imagine that each of the 4 string grids have a grid size of N^2 , the location of the string of each would be at $(N/2, N/2)$. These grids would then be combined together to form figure 3.17.

However, if one of the four original string grids were moved away from the centre to a location of $(7/8, N/2)$, then the angle distribution in that grid is modified. When the grids merge together, there will be an unnatural θ discontinuity between the modified grid and the 3 unchanged grids as seen in figure 3.19. This discontinuity in

particular is something the Universe would never allow to occur, and the evolution of the field from this point does not behave as it should when compared to PQ and QCD epoch simulations.

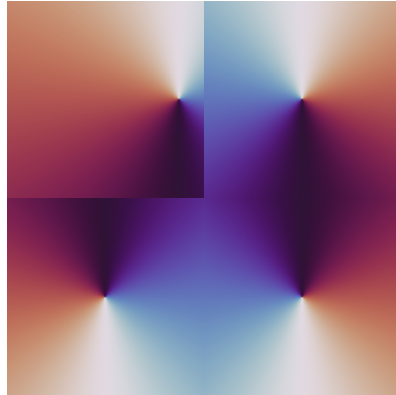
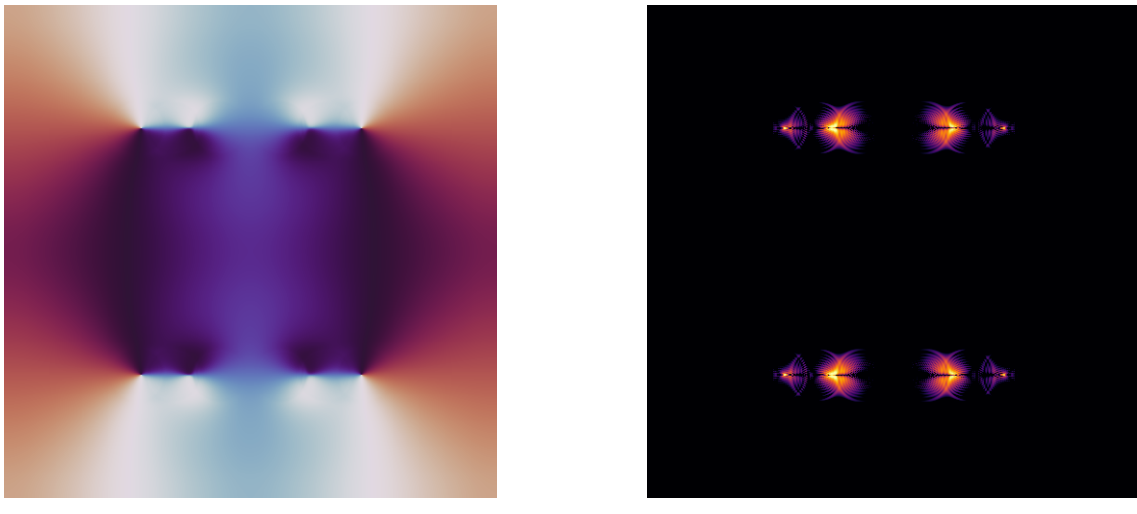


Figure 3.19: The discontinuity in the θ distribution in this initial condition is unnatural. Field interactions would not allow such a discontinuity to be formed.

Thus, we require the movement of the location of the string whilst maintaining the angle distribution of a centre string so that at the edges of the grid. This configuration, when grids are merged together will not possess an angle discontinuity. To create figure 3.18, we scale the angle distribution of the offset string with the angle distribution of the centre string. At the location of the offset, the angle distribution will behave as expected. However, for lattice points away and closer to the edge of the grid, the angle distribution of the original string becomes dominant. At the boundaries for the grid, there is no effectively no angle contribution of the offset string, and there is no longer any discontinuity in the angle distribution.

By the geometry of the system when the string is offset and placed at $(7N/8, N/2)$, two additional strings are forced to appear in order to maintain a continuity in angle. We perform this offset four times for the initial starting point in figure 3.18.



(a) θ distribution around the field

(b) Axion energy density $\ln(\rho_a/\bar{\rho}_a)$.

Figure 3.20: The strings of opposite chirality have ended up colliding. We can see that the strings that were not involved in the collision has also been pulled along more towards the centre. The movement of strings is accompanied by an emission of energy in the form of axions.

The strings of opposite chirality end up colliding despite there being no coupling to QCD. This implies that an attractive force exists between two strings of opposite chirality. It can be seen in figure 3.20 compared to figure 3.18 that the 4 outer strings have been pulled inwards towards the centre due to the opposite chirality strings directly adjacent to them. This also explains why the 4 strings configuration in figure 3.17 is stable in a periodic grid. The attractive and repelling forces that each string exerts on one another are balanced. Thus, the strings will not move. It has also been noticed in figure 3.20b that as strings move to allow for a more stable

field configuration, they emit axions.

2D simulations could be seen as effectively a slice of a 3D simulation. The opposite chirality strings in 2D are actually just two single points of a string loop in 3D. String loops have a tension which naturally pulls it together, emitting axions while they shrink and decay away [32]. Thus, providing a reason why strings emit axions as they move toward each other in the 2D simulation.

To summarise what we have learned about the string dynamics,

- As strings move, they emit axions.
- Strings are locations of high energy density in the axion field.
- Strings of opposite chirality seem to possess an attractive force between each other.
- When two strings collide, a lot of energy in the axion field stored in strings is converted to the saxion field.
- Axion coupling to QCD accelerates the collapse of the axion string network via the surface tension on domain walls which connect two strings

3.5 Oscillons

Oscillons are quasi stable objects that occur naturally and are solutions to the Sine-Gordon equation for an angular field in an expanding Universe [65] in equation 2.17. They are locations where the axion self-interactions are balanced against the effect of the expanding Universe [16]. This is because in these simulations, there exist a brief period whereby the term $\min(\eta, \eta_c)^n$ is increasing. This non-linearity arises because the axion mass grows until its zero-temperature mass has been reached. Oscillons form in the brief epoch when the axion mass is still growing and the cutoff temperature T_c and time $\hat{\eta}_c$ has not yet been reached.

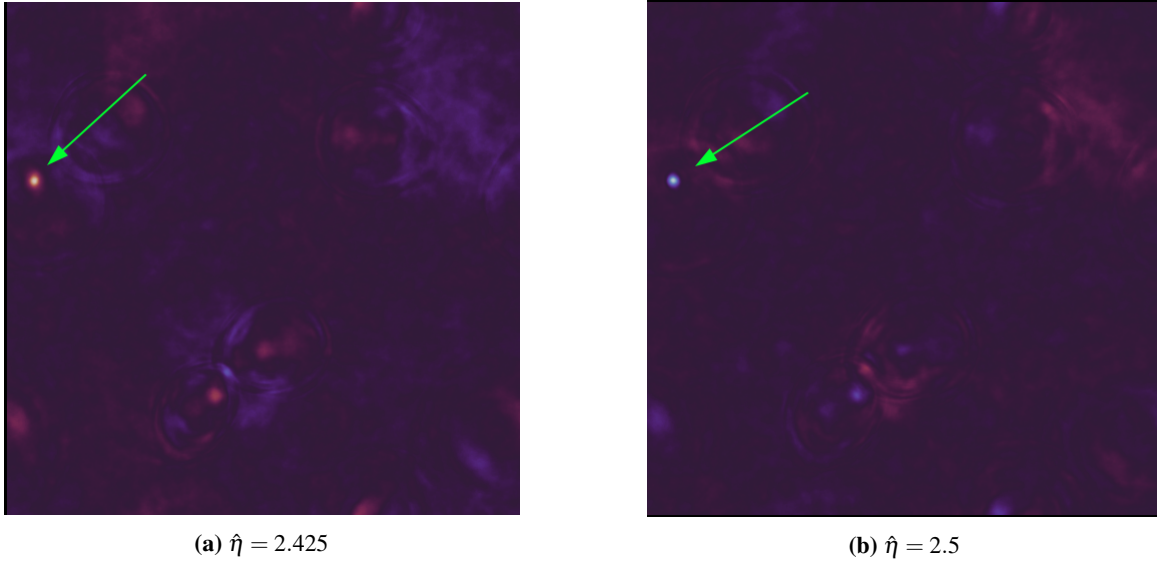


Figure 3.21: The distribution of θ for the field is plotted. Oscillons can be observed as locations where the field oscillates about $\theta = 0$. This can be seen with certain regions of the field continuously oscillating between blue and red.

From now on, the simulations are of the QCD epoch with $n = 6.68$ and $\lambda = 1024$. The string network has completely collapsed by $\hat{\eta} = 2.1$ and thus, the cutoff time for axion mass growth $\hat{\eta}_c = 2.8, 3.6$ and 6.0 does not play a role in the collapse of the axion string network. All three simulations look the same until each cutoff time is reached. For example, when $\hat{\eta} = 2.8$, the $\hat{\eta}_c = 3.6$ and 6.0 simulations will still be the same but will diverge from the $\hat{\eta}_c = 2.8$ simulation.

Visually, oscillons appear as regions in the field which have values that oscillate about $\theta = 0$. This can be seen in figure 3.21, where the field constantly oscillates between blue and red. They are locations within

the field where unlike the rest of the field whose $\theta = 0$, the axion remains excited and maintain much larger amplitudes of θ oscillation compared to the rest of the field.

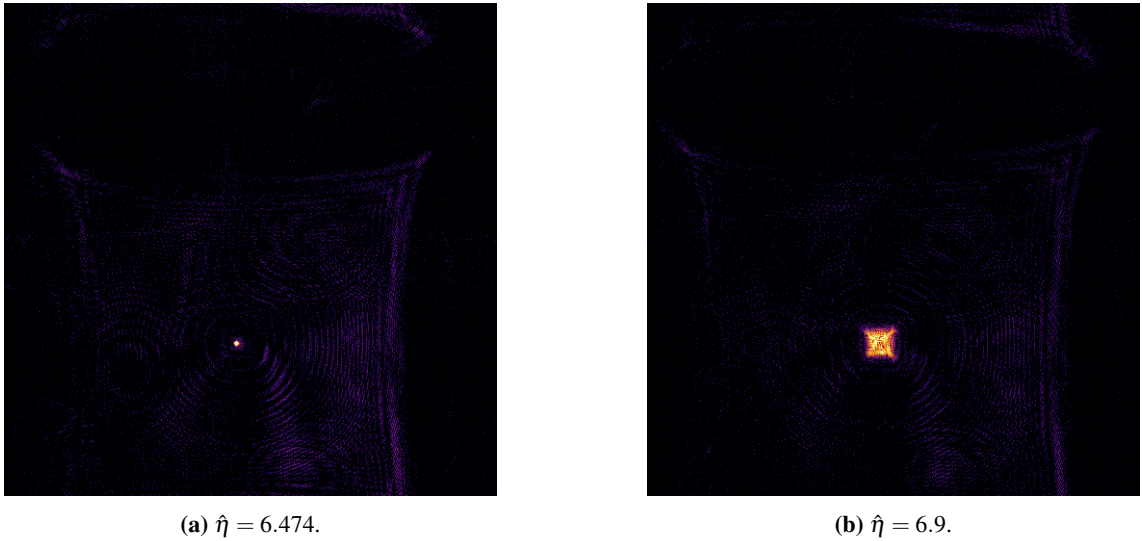


Figure 3.22: Energy density of the field at different points in time. Energy density is maintained in a single position for a long time after the cutoff time $\hat{\eta}_c = 2.8$ has been past. Around $\hat{\eta} = 6.7$, the over dense regions due to oscillons expand, giving rise to less dense overdensities. Note that at $\hat{\eta} = 6.9$ in figure 3.22b, the overdensity is still expanding.

In figure 3.22, only very few oscillons are able to form. This is because for the $\hat{\eta}_c = 2.8$ case, the cutoff time for axion mass growth is shorter. This means there is less time for oscillons to emerge as solutions to the non-linear EOMs. That oscillons maintains the energy density within a certain region of the field for a long period of time past the cutoff time η_c as seen figure 3.22a. However, once the axion mass growth period ends, we can see that eventually the oscillon is unstable and its energy slowly expands as seen in figure 3.22b. This is proof that oscillons are stabilised against the gradient pressure and the expansion of the Universe by their growing axion mass. They eventually must become unstable as the axion mass stops growing. The end result is less energy dense overdensities compared to the oscillon that proceeded it.

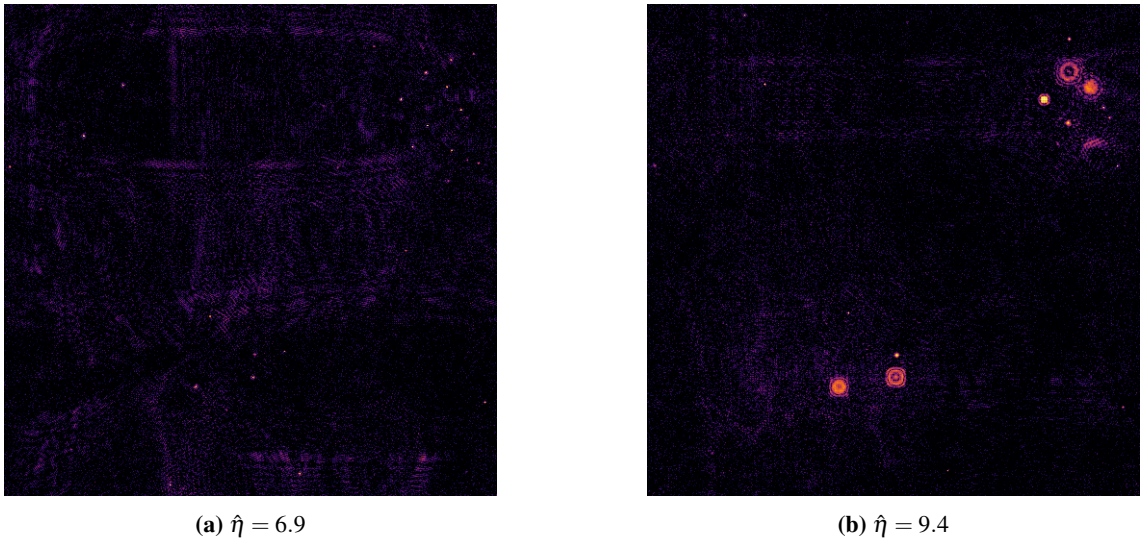


Figure 3.23: Energy density of the field at different points in time in a $\hat{\eta}_c = 3.6$ simulation. There is a larger quantity of oscillons compared to the $\hat{\eta}_c = 2.8$ scenario. However, it can be noted that at $\hat{\eta} = 9.4$, some oscillons have dissipated, allowing their overdense regions to expand to a certain size. However, some oscillons still remain at this time.

More time is allowed for oscillons to form in figure 3.23. The size of these oscillons are smaller than the oscillon in figure 3.22. Some oscillons have dissipated at $\hat{\eta} = 9.4$ as seen in figure 3.23b. These overdensities

seem to expand to a characteristic size dependent on the properties of the original oscillon as they do not expand to the same size.

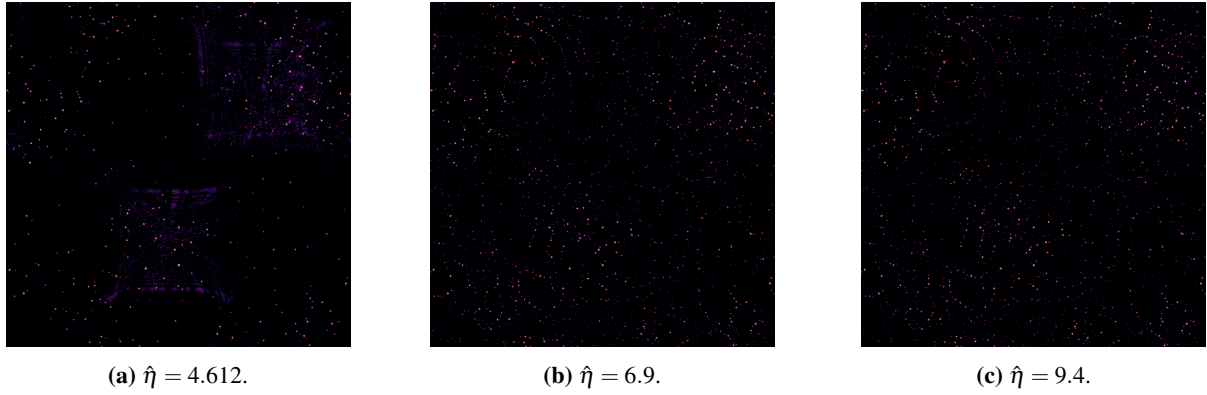


Figure 3.24: Energy density of the field at different points in time for the $\hat{\eta}_c = 6.0$ simulation. Despite further evolution of the field to later times in figure 3.24c, there is basically no change in the distribution of energy density from $\hat{\eta}_c = 6.9$ to 9.4.

From 3.24, we observe that a whole slew of oscillons form. Moreover, oscillons only appear at the location of the collapsed strings and where domain walls used to be as seen in figure 3.15. There are large regions of the field with no energy overdensities. We can see from figures 3.22, 3.23 and 3.24, that the larger the zero-temperature mass is, the more oscillons form. These oscillons will persist for long periods of time after the cutoff time η_c as we see no apparent change in the distribution of energy density when comparing figures 3.24b and 3.24c.

Evolving for longer periods of time sees the oscillon dissipate, and the overdense region left behind will have its energy expand. As a consequence of oscillon dynamics caused by a brief epoch of non-linear field evolution, different axion masses will change the distribution of energy density.

Another property of the oscillon to explore is the oscillon radius which was found by Buschmann et al. [16] to follow the relation $r \sim m_a(T)^{-1}$. This means that from the time between figure 3.24a to figure 3.24b, the size of the oscillon is meant to decrease. This seems to be the case in our simulations. However, the relation $r \sim m_a(T)^{-1}$ in particular cannot be gleaned from our simulations. This is because of the 512^2 size of the simulation. More lattice points are required in order to examine this relation.

3.6 Manufactured Oscillons

Oscillons were manually created using the equation [52]

$$\theta(t=0, r) = \frac{A}{\cosh(r/\sigma)}, \quad \dot{\theta}(t=0, r) = 0, \quad (3.6)$$

where A and σ are free parameters that control the amplitude and radius of the initial angle perturbation that is created.

Due to these initial conditions, the axion-only EOMs are used as there is no radial mode to be calculated. Thus, this simulation uses the late time EOM from equation 2.17. We use the initial time of $\hat{\eta}_i = 1.7$ in the QCD epoch. This allows us to focus on the effect of changing η_c on an isolated oscillon. $\lambda = 1024, n = 6.68$ for these simulation. The energy density of θ is

$$\rho_\theta = \frac{1}{2}\dot{\theta}^2 + \frac{1}{2}(\nabla\theta)^2 + V(\theta). \quad (3.7)$$

However, we will be once again be only look at $\rho' = \rho_\theta - V(\theta)$.

What we examine are not oscillons specifically, but the overdense regions as a result of the oscillon. We chose unique initial conditions where $A = 2$ and $\sigma = 1$ in order to accelerate the process whereby the overdensities form for a 256^2 sized grid. It was found that for larger choices of σ , the oscillon in the simulation will persist and maintain the energy density within a region for longer periods of time than we are willing to simulate.

However, for small choices of σ , the oscillon seemingly dissipates much quicker and the highly energy dense region will expand to a characteristic size dependent on $\hat{\eta}_c$. This is because the initial oscillon that was inserted into the simulation are the same for all three simulations.

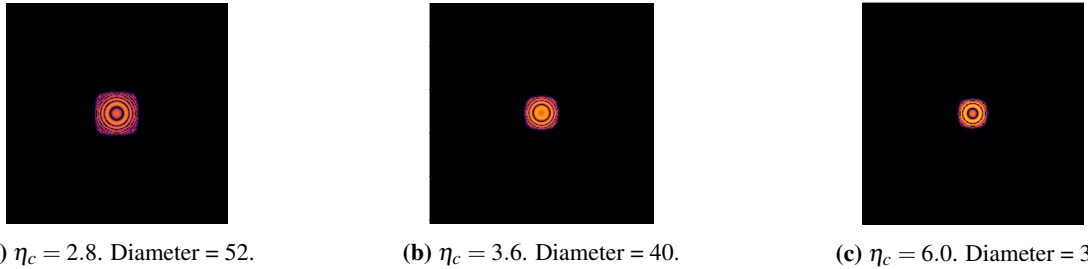


Figure 3.25: A plot of the energy density of the theta field $\ln(\rho'/\bar{\rho}')$ at $\hat{\eta} = 8.9$. A larger zero-temperature axion mass will lead to a smaller but more energy dense overdensity. The diameter of the overdensity is measured in lattice points.

The same initial conditions are used for each of the three overdensities. A larger zero-temperature axion mass will lead to a smaller overdensity. This means that the energy density of the field will be localised into smaller regions making it more energy dense. Analysis must be done with larger simulations to determine the relation between the axion mass and the size of the resulting overdense region.

To summarise the physics of oscillons

- Oscillons are naturally occurring solutions to a non-linear EOM during the brief period of time when the axion mass is growing.
- Oscillons form at the locations of collapsed strings and domain walls which are regions of higher energy density.
- Oscillons will maintain this highly energy dense regions for long periods of time after the cutoff temperature T_c and cutoff time $\hat{\eta}_c$ has already been past.
- In this model, a larger axion mass equates to a longer period of axion mass growth, allowing for the quantity of oscillons that emerge to increase.
- A larger axion mass seems to result in a smaller radius for oscillons, thus, causing the same amount of energy to be compactified into smaller regions.
- Eventually, long after the zero-temperature axion has been reached, these overdense regions previously maintained by oscillons will expand. This reduces the degree of overdensity, though a region of high energy density will still remain.

These regions of high energy density from oscillons are significant, as they will collapse into axion miniclusters [65]. These miniclusters will then grow linearly before beginning to merge and form dark matter mini halos. Therefore, low mass high density clumps of gravitationally bound axions can form part of the dark matter density in the universe. At the present, most of the axion population could be contained within these clusters [26]. The distribution of axionic dark matter would be expected to be inhomogeneous in the post-inflationary PQ symmetry breaking scenario. In this model, the larger the axion mass, the larger the degree of clumping will be observed as energy is localised in smaller regions. There will be some inhomogeneities in the pre-inflationary PQ symmetry breaking scenario, though not nearly to the same degree.

Chapter 4

Implications

4.1 Detection

Experiments aiming to detect the axion rely heavily on its couplings to the SM. The interaction Lagrangian which is applicable for the low temperature Universe today is [47]

$$\mathcal{L}_{\text{int}} = -\frac{g_{a\gamma}}{4} a F_{\mu\nu} \tilde{F}^{\mu\nu} + \frac{g_{aN}}{2m_N} \partial_\mu a (\bar{N} \gamma^\mu \gamma_5 N) + \frac{g_{ae}}{m_e} \partial_\mu a (\bar{e} \gamma^\mu \gamma_5 e) - \frac{i}{2} g_{da} \bar{N} \sigma_{\mu\nu} \gamma_5 N F^{\mu\nu}, \quad (4.1)$$

where $\sigma^{\mu\nu} = i/2[\gamma^\mu, \gamma^\nu]$, a is the axion, γ is the photon, e is the electron and N refers to a nucleon. This Lagrangian equation 4.1 means the axion has a coupling to electromagnetism of

$$a \mathbf{E} \cdot \mathbf{B} = -a F_{\mu\nu} \tilde{F}^{\mu\nu} / 4. \quad (4.2)$$

This allows the axion to convert into photons in the presence of an external magnetic field via the Primakoff process 4.1.

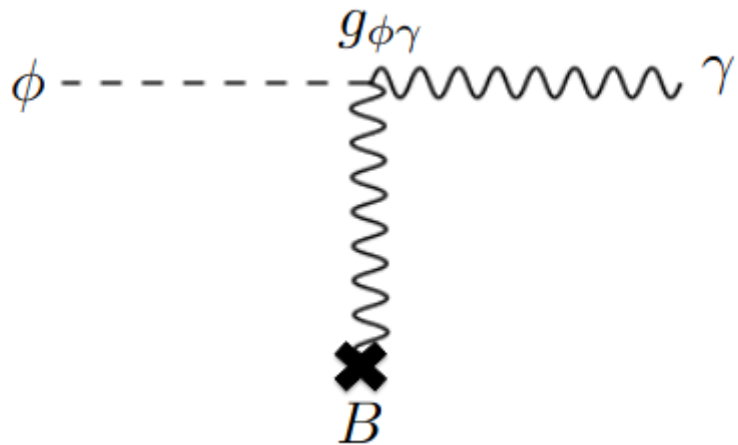


Figure 4.1: Axion photon interaction induced by an external magnetic field via the Primakoff interaction [47]. This mechanism allows for the detection of axions sourced from the sun with the probability of axion photon conversion increasing with the path length.

Many experiments such as dark matter haloscopes can only search for an axion within a certain mass range. We can see this from the parameter space they probe in figure 1.7. Given that a large cost and experimental effort is being undertaken in the search for the axion, it is necessary to predict the expected mass range of the axion. However, in the scenario where $U(1)_{\text{PQ}}$ symmetry is broken after inflation, topological defects such as strings and domain walls arise, complicating the calculation of the axion mass. Computer simulations use the axion mass as a free parameter to determine for what mass ranges the observed dark matter abundance is achieved in the scenario where axions are dark matter. Our simulations also predict that the inhomogeneities of dark matter distribution will change depending on the zero-temperature axion mass.

If axion miniclusters form as predicted by axion simulations and have survived to today, we can predict their size, density and how they interact gravitationally with regular baryonic matter. Dark matter haloscope experiments such as ADMX [40] and HAYSTAC [24] are the primary method to probe for axions if they are to make up dark matter. These experiments are conducted on Earth, waiting for dark matter of the Milky Way Halo to collide with the Earth. If all axion dark matter are bound in miniclusters [26], this could be problematic for haloscope experiments. The rate at which the Earth would collide with an axion minicluster could be so low as to be once every 100,000 years [37]. An axion minicluster collision with the Earth would be very rare and thus, other axion detection experiments are important.

One promising approach to search for axion miniclusters is to focus on axion minicluster interactions with neutron stars. These experiments rely on the axion-photon coupling which allows the axion to convert into photons in the presence of an external magnetic field. The stronger the magnetic field is, the more probable the interaction is to occur. Hence, rather than solely relying on gravitational methods to detect dark matter, this experiment would rely on the strong magnetic fields generated by neutron stars [25]. The experiment would search for dark matter and simultaneously uncover its nature as at least being partly made up of axions.

The power per solid angle generated by an axion minicluster neutron star interaction is predicted by the Goldreich-Julian model [31] to be

$$\frac{d\mathcal{P}_a}{d\Omega} \sim \frac{\pi}{3} g_{a\gamma\gamma}^2 B_0^2 \frac{R_{NS}^6}{R_c^3} \frac{\rho_a}{m_a} \quad (4.3)$$

where ρ_a is the axion density at the conversion radius, $g_{a\gamma\gamma}$ is the axion-photon coupling, R_{NS} is the neutron star radius and R_c is the radius at which axions resonantly convert into photons.

The power scales with B_0^2 which is the strength of the magnetic field generated by the neutron stars at its poles. Thus, a higher flux of photons than expected may be detected when viewing neutron stars. With simulations, the amount of photon flux from axion minicluster neutron star interactions could be predicted using equation 4.3. This could be the a viable way to observe the axion if the axion population were bound up inside these dark miniclusters.

Axion helioscopes also use the axion-photon coupling to search for ALPs produced by the sun [53]. These experiments can be used to determine if an axion is indeed produced in nature. They currently do not probe the parameter space near the QCD band in figure 1.7. As of writing, IAXO has not yet been built, but it is a promising helioscope project with highly ambitious goals. IAXO may be sensitive enough to search for the QCD axion in the $1 \text{ meV} \sim 1 \text{ eV}$ mass range [9] and other elusive ALPs.

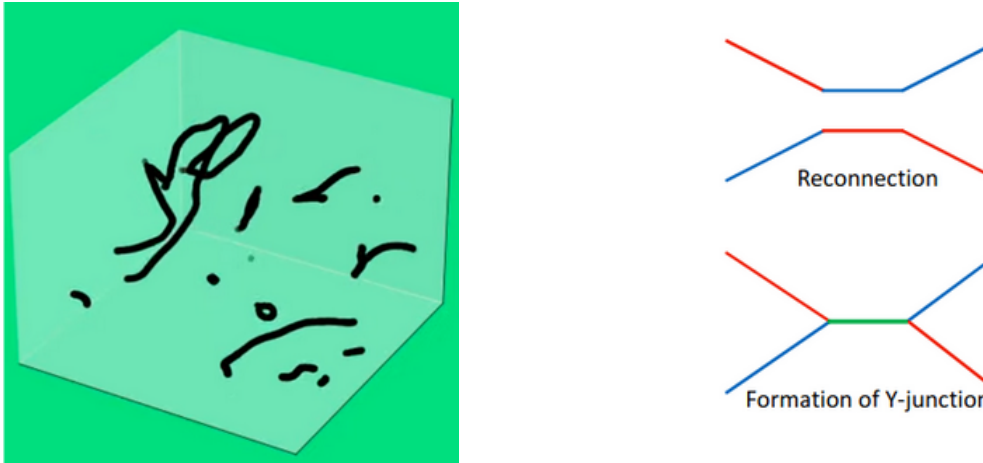
Thus, it is necessary to use simulations to determine what axion mass generates the right dark matter abundance. If axions are dark matter, this axion mass can change the way dark matter is distributed within halos as seen in our simulations. Simulations can help inform the amount of photon flux which is expected from axion minicluster and neutron star interactions, making them critical to the search for the axion.

4.2 Future Research

There are many ideas that could be explored. To begin with, what makes up an axion minicluster is not well defined. Thus, it could be interesting to perform Monte Carlo simulations which track the structure of axion miniclusters over time to see how they could be categorised quantitatively [39]. Subsequent N-body simulation could be performed and its gravitational influence on regular baryonic matter such as a star could be investigated [26].

What this thesis has explored is the simulation of an effective axion model. However, there are different axion models which may be explored. Recently there have been papers that explore unique ideas in the DFSZ model. This is a model which introduces an additional Higgs field and the complex scalar PQ ψ field. Essentially, they state that axion strings with electroweak gauge flux in the DFSZ model may not follow the ‘scaling solution’ [5]. Their model predicts a stable superconducting string which permits a supercurrent to flow through it, inducing an attractive force between two topological strings of the same topological charge. This allows novel string shapes to appear such as the Y-junction [12] and opens up the possibility that when two strings meet, they do not necessarily reconnect with each other with probability of order unity. Shrinking string loop dynamics may be different and attain a stable form called vortons, supported by the electromagnetic force of the string

current rather than disappear [29]. Thus, future simulations investigating this DFSZ axion model are required as much of its dynamics remain unexplored.



(a) Visualising a simulation in 3D. There are strings and loops present.

(b) The formation of a Y-junction in the DFSZ model [5].

Figure 4.2: In 3D, if two strings collide, there is an 100% chance of reconnection. However, in this DFSZ model, a Y-junction may form.

Another recent update to the axion model may be the requirement of a companion axion [19]. This paper identifies that the axion solution to the strong CP problem relies on the axion potential being dominated by QCD instantons that break a 4D global $U(1)_{\text{PQ}}$ symmetry [8]. However, this can be spoiled by additional sources of PQ symmetry breaking which can come from coloured gravitational instantons [18]. Thus, another CP-violating parameter denoted as θ_g must be accounted for due to coloured gravitational instantons. This problem can be solved by introducing another companion axion which dynamically drives θ_g to zero, just like the regular axion. In this model, there are two QCD axions and two free parameters f_a and f'_a . Then if we assume that the dark matter abundance is axions, it may be a sum of two axion abundances $\Omega_{\text{DM}} = \Omega_{a1} + \Omega_{a2}$. If we assume that one of the axions is lighter than the other as a consequence of their different decay constants $\epsilon = f_a/f'_a$, perhaps only one axion will be able to be detected by dark matter haloscope experiments as seen in figure 4.3. For this model, the parameter space of the QCD axion will be different to what the DFSZ and KSFZ models predict.

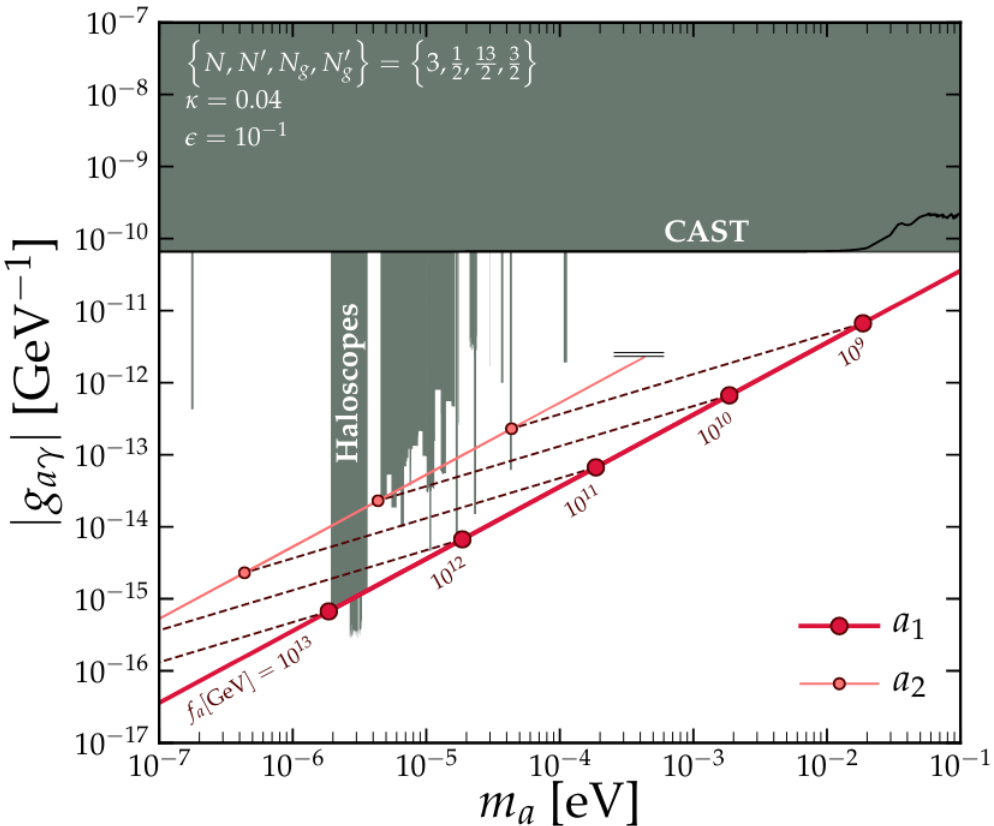


Figure 4.3: Axion-photon coupling for the axion (a_1) and a companion axion (a_2). The dashed lines is to emphasise the connection between the two axion mass eigenstates set by $\epsilon = f_a/f'_a = 10^{-1}$. The lighter axion a_2 is much easier to probe through axion haloscope experiments [19].

Another theory attributes the global $U(1)_{\text{PQ}}$ symmetry breaking in four dimensions to the breaking of a local $U(1)_{\text{PQ}}$ symmetry breaking in five dimensions [30]. Normally it is assumed that QCD coupling remains asymptotically free at extremely high energies of the early Universe (UV) and QCD dynamics are unchanged under the Planck scale. This is a UV theory which modifies QCD dynamics. As a consequence, 5D instantons would enhance the axion mass. This theory would predict a much heavier axion which may be difficult to explore via experiment.

I would like to draw parallels of this particular idea to the state of Supersymmetry (SUSY) in Dark Matter physics. SUSY provides an easy weakly-interacting-matter-particle (WIMP) which could be dark matter [46]. However, as of writing, no such WIMP has been found by experiment. This has led some to rule out SUSY as a viable theory to produce a dark matter candidate as the SUSY parameter space becomes increasingly constrained over time. However, many theories are still being formulated today to explain and ‘protect’ SUSY particles from being found by collider experiments by predicting a larger mass for these particles than for the minimal supersymmetric model. Similar theories for the axion may be required to preserve the axion as a dark matter candidate if experiments provide a null detection result.

Different axion models introduce novel ideas which consequently generate different string dynamics and axion masses. If they are correct, it may be that experiments are probing the wrong regions of the parameter space or perhaps a whole host of axions exist in nature. Thus, it is necessary to continue to use simulations in order to explore different axion models and their effect on the cosmology of the Universe.

Chapter 5

Conclusion

This project explored the interesting ramifications to cosmology if axions are to be included as an extension to the SM. Axions are scalar particles originally designed to the strong CP problem which are also great dark matter candidates that only very weakly interact with the SM. If axions are dark matter, simulations are critical to understanding how the distribution of dark matter is modified. If $U(1)_{\text{PQ}}$ symmetry is broken after inflation, topological defects such as strings and domain walls will remain and complicate the calculation of the specific axion mass which generates the observed dark matter abundance.

In this thesis, we have explored the dynamics of strings and oscillons. Power spectrum analyses are used to study how energy is stored in strings and domain walls and how that energy gets distributed when two strings collide due to an attractive force for strings of opposite chirality. Oscillons appear during a brief epoch when the axion mass is growing. Interestingly, oscillons in our simulations lead to large energy overdensities which may collapse into axion miniclusters. Thus, if dark matter is comprised of axions, then our simulations would predict that dark matter halos have an inhomogeneous matter distribution. The degree of these inhomogeneities is directly influenced by the chosen axion mass.

The prediction of axions being gravitationally bound in miniclusters may influence dark matter axion detection experiments. One promising approach may be to focus on axion minicluster and neutron star interactions via the axion-photon coupling. Simulations may be key in predicting the photon flux expected from these interactions. Future work may include simulating different axion models which predict different couplings or even novel string dynamics which remain largely unexplored.

Appendix A

Appendix

The simulation code for this project can be found at the link: <https://github.com/MaxJXiao/Cosmic-Strings>.

Bibliography

- [1] *More images of 1e 0657-56*, <https://chandra.harvard.edu/photo/2006/1e0657/more.html>, Accessed: 2021-11-12.
- [2] *The origins of the universe: Cosmic defects*, http://www.ctc.cam.ac.uk/outreach/origins/cosmic_structures_two.php, Accessed: 2021-11-6.
- [3] *Proton beams are back in the lhc*, <https://home.cern/news/news/accelerators/proton-beams-are-back-lhc>, Accessed: 2021-11-8.
- [4] G. Aad, T. Abajyan, B. Abbott, J. Abdallah, S. Abdel Khalek, A.A. Abdelalim, O. Abdinov, R. Aben, B. Abi, M. Abolins, and et al., *Observation of a new particle in the search for the standard model higgs boson with the atlas detector at the lhc*, Physics Letters B **716** (2012), no. 1, 1–29.
- [5] Yoshihiko Abe, Yu Hamada, and Koichi Yoshioka, *Electroweak axion string and superconductivity*, Journal of High Energy Physics **2021** (2021), no. 6.
- [6] C. Abel, S. Afach, N.J. Ayres, C.A. Baker, G. Ban, G. Bison, K. Bodek, V. Bondar, M. Burghoff, E. Chanel, and et al., *Measurement of the permanent electric dipole moment of the neutron*, Physical Review Letters **124** (2020), no. 8.
- [7] Iminhaji Ablimit, Gang Zhao, Chris Flynn, and Sarah A. Bird, *The rotation curve, mass distribution, and dark matter content of the milky way from classical cepheids*, The Astrophysical Journal **895** (2020), no. 1, L12.
- [8] James Alvey and Miguel Escudero, *The axion quality problem: global symmetry breaking and wormholes*, Journal of High Energy Physics **2021** (2021), no. 1.
- [9] E. Armengaud, D. Attié, S. Basso, P. Brun, N. Bykovskiy, J.M. Carmona, J.F. Castel, S. Cebrián, M. Cicoli, M. Civitani, and et al., *Physics potential of the international axion observatory (iaxo)*, Journal of Cosmology and Astroparticle Physics **2019** (2019), no. 06, 047–047.
- [10] K. Basu, C. Hernández-Monteagudo, and R. A. Sunyaev, *Cmb observations and the production of chemical elements at the end of the dark ages*, Astronomy and Astrophysics **416** (2004), no. 2, 447–466.
- [11] Gianfranco Bertone and Dan Hooper, *History of dark matter*, Reviews of Modern Physics **90** (2018), no. 4.
- [12] Luís M. A. Bettencourt, Pablo Laguna, and Richard A. Matzner, *Nonintercommuting cosmic strings*, Physical Review Letters **78** (1997), no. 11, 2066–2069.
- [13] Kfir Blum, Raffaele Tito D’Agnolo, Mariangela Lisanti, and Benjamin R. Safdi, *Constraining axion dark matter with big bang nucleosynthesis*, Physics Letters B **737** (2014), 30–33.
- [14] Sz. Borsanyi, Z. Fodor, K. H. Kampert, S. D. Katz, T. Kawanai, T. G. Kovacs, S. W. Mages, A. Pasztor, F. Pittler, J. Redondo, A. Ringwald, and K. K. Szabo, *Lattice qcd for cosmology*, 2016.
- [15] Malte Buschmann, Joshua W. Foster, Anson Hook, Adam Peterson, Don E. Willcox, Weiqun Zhang, and Benjamin R. Safdi, *Dark matter from axion strings with adaptive mesh refinement*, 2021.

- [16] Malte Buschmann, Joshua W. Foster, and Benjamin R. Safdi, *Early-universe simulations of the cosmological axion*, Physical Review Letters **124** (2020), no. 16.
- [17] Francesca Chadha-Day, John Ellis, and David J. E. Marsh, *Axion dark matter: What is it and why now?*, 2021.
- [18] Zhe Chen and Archil Kobakhidze, *Coloured gravitational instantons, the strong cp problem and the companion axion solution*, 2021.
- [19] Zhe Chen, Archil Kobakhidze, Ciaran A. J. O’Hare, Zachary S. C. Picker, and Giovanni Pierobon, *Phenomenology of the companion-axion model: photon couplings*, 2021.
- [20] Douglas Clowe, Maruša Bradač, Anthony H. Gonzalez, Maxim Markevitch, Scott W. Randall, Christine Jones, and Dennis Zaritsky, *A direct empirical proof of the existence of dark matter*, The Astrophysical Journal **648** (2006), no. 2, L109–L113.
- [21] Karen Crowther and Niels Linnemann, *Renormalizability, fundamentality and a final theory: The role of uv-completion in the search for quantum gravity*, 2017.
- [22] Christopher Dessert, Andrew J. Long, and Benjamin R. Safdi, *No evidence for axions from chandra observation of magnetic white dwarf*, 2021.
- [23] Michael Dine, Willy Fischler, and Mark Srednicki, *A simple solution to the strong CP problem with a harmless axion*, Physics Letters B **104** (1981), no. 3, 199–202.
- [24] Alex G. Droster and Karl van Bibber, *Haystac status, results, and plans*, 2019.
- [25] Thomas D. P. Edwards, Bradley J. Kavanagh, Luca Visinelli, and Christoph Weniger, *Transient radio signatures from neutron star encounters with qcd axion miniclusters*, 2020.
- [26] Benedikt Eggemeier, Javier Redondo, Klaus Dolag, Jens C. Niemeyer, and Alejandro Vaquero, *First simulations of axion minicluster halos*, Physical Review Letters **125** (2020), no. 4.
- [27] Benedikt Eggemeier, Bodo Schwabe, Jens C. Niemeyer, and Richard Easther, *Gravitational collapse in the post-inflationary universe*, 2021.
- [28] Cyrus Faroughy, *Cosmological perturbations in a universe with a domain wall era*, 2018.
- [29] Hajime Fukuda, Aneesh V. Manohar, Hitoshi Murayama, and Ofri Telem, *Axion strings are superconducting*, Journal of High Energy Physics **2021** (2021), no. 6.
- [30] Tony Gherghetta, Valentin V. Khoze, Alex Pomarol, and Yuri Shirman, *The axion mass from 5d small instantons*, Journal of High Energy Physics **2020** (2020), no. 3.
- [31] Peter Goldreich and William H. Julian, *Pulsar Electrodynamics*, Astrophysical Journal **157** (1969), 869.
- [32] Marco Gorgetto, Edward Hardy, and Giovanni Villadoro, *More axions from strings*, SciPost Physics **10** (2021), no. 2.
- [33] Tetsutaro Higaki, Kwang Sik Jeong, Naoya Kitajima, Toyokazu Sekiguchi, and Fuminobu Takahashi, *Topological defects and nano-hz gravitational waves in aligned axion models*, Journal of High Energy Physics **2016** (2016).
- [34] Peter W. Higgs, *Broken symmetries and the masses of gauge bosons*, Phys. Rev. Lett. **13** (1964), 508–509.
- [35] G. Hinshaw, J. L. Weiland, R. S. Hill, N. Odegard, D. Larson, C. L. Bennett, J. Dunkley, B. Gold, M. R. Greason, N. Jarosik, and et al., *Five-year wilkinson microwave anisotropy probe observations: Data processing, sky maps, and basic results*, The Astrophysical Journal Supplement Series **180** (2009), no. 2, 225–245.
- [36] Anson Hook, *Tasi lectures on the strong cp problem and axions*, 2021.

- [37] Igor G. Irastorza and Javier Redondo, *New experimental approaches in the search for axion-like particles*, Progress in Particle and Nuclear Physics **102** (2018), 89–159.
- [38] A.H. Jaffe, *Cosmology 2012: Lecture notes*, (2012).
- [39] Bradley J. Kavanagh, Thomas D. P. Edwards, Luca Visinelli, and Christoph Weniger, *Stellar disruption of axion miniclusters in the milky way*, 2020.
- [40] R. Khatriwada, D. Bowring, A. S. Chou, A. Sonnenschein, W. Wester, D. V. Mitchell, T. Braine, C. Bartram, R. Cervantes, N. Crisosto, N. Du, S. Kimes, L. J Rosenberg, G. Rybka, J. Yang, D. Will, G. Carosi, N. Woollett, S. Durham, L. D. Duffy, R. Bradley, C. Boutan, M. Jones, B. H. LaRoque, N. S. Oblath, M. S. Taubman, J. Tedeschi, John Clarke, A. Dove, A. Eddins, A. Hashim, S. R. O’Kelley, S. Nawaz, I. Siddiqi, N. Stevenson, A. Agrawal, A. V. Dixit, J. R. Gleason, S. Jois, P. Sikivie, N. S. Sullivan, D. B. Tanner, J. A. Solomon, E. Lentz, E. J. Daw, M. G. Perry, J. H. Buckley, P. M. Harrington, E. A. Henriksen, K. W. Murch, and G. C. Hilton, *Axion dark matter experiment: Detailed design and operations*, 2020.
- [41] Jihn Kim, *Axionic domain wall number related to $u(1)_{\text{anom}}$ global symmetry*, Physics Letters B **759** (2016).
- [42] Jihn E. Kim, *Weak-interaction singlet and strong CP invariance*, Phys. Rev. Lett. **43** (1979), 103–107.
- [43] Jihn E. Kim, *Light pseudoscalars, particle physics and cosmology*, Physics Reports **150** (1987), no. 1, 1–177.
- [44] Edward W. Kolb and Igor I. Tkachev, *Axion miniclusters and bose stars*, Physical Review Letters **71** (1993), no. 19, 3051–3054.
- [45] J. Kuckei, C. Dib, A. Faessler, T. Gutsche, S. G. Kovalenko, V. E. Lyubovitskij, and K. Pumsa-ard, *Strong cp violation and the neutron electric dipole form factor*, Physics of Atomic Nuclei **70** (2007), no. 2, 349–357.
- [46] Jeanette Miriam Lorenz, *Supersymmetry and the collider dark matter picture*, Modern Physics Letters A **34** (2019), no. 30, 1930005.
- [47] David J.E. Marsh, *Axion cosmology*, Physics Reports **643** (2016), 1–79.
- [48] Ken Mimasu and Verónica Sanz, *Alps at colliders*, 2015.
- [49] Ben Moore, Sebastiano Ghigna, Fabio Governato, George Lake, Thomas Quinn, Joachim Stadel, and Paolo Tozzi, *Dark matter substructure within galactic halos*, The Astrophysical Journal **524** (1999), no. 1, L19–L22.
- [50] S. Naoz and R. Barkana, *Growth of linear perturbations before the era of the first galaxies*, Monthly Notices of the Royal Astronomical Society **362** (2005), no. 3, 1047–1053.
- [51] Ciaran O’HARE, *cajohare/axionlimits: Axionlimits*, July 2020.
- [52] Jan Ollé, Oriol Pujolàs, and Fabrizio Rompineve, *Recipes for oscillon longevity*, Journal of Cosmology and Astroparticle Physics **2021** (2021), no. 09, 015.
- [53] Ciaran A.J. O’Hare, Andrea Caputo, Alexander J. Millar, and Edoardo Vitagliano, *Axion helioscopes as solar magnetometers*, Physical Review D **102** (2020), no. 4.
- [54] R. D. Peccei and Helen R. Quinn, *CP conservation in the presence of pseudoparticles*, Phys. Rev. Lett. **38** (1977), 1440–1443.
- [55] Roberto D. Peccei, *The strong cp problem and axions*, Axions (2008), 3–17.
- [56] Annika Peter, *Dark matter: A brief review*, (2012).
- [57] W H Press, B S Ryden, and D N Spergel, *Dynamical evolution of domain walls in an expanding universe*, Astrophysical Journal; (USA) **347** (1989).

- [58] J I Read, *The local dark matter density*, Journal of Physics G: Nuclear and Particle Physics **41** (2014), no. 6, 063101.
- [59] Nirakar Sapkota and Binod Adhikari, *A review on cosmic inflation*, International Journal of Current Research and Academic Review **5** (2017).
- [60] J. A. Schewtschenko, C. M. Baugh, R. J. Wilkinson, C. Bøhm, S. Pascoli, and T. Sawala, *Dark matter–radiation interactions: the structure of milky way satellite galaxies*, Monthly Notices of the Royal Astronomical Society **461** (2016), no. 3, 2282–2287.
- [61] Pierre Sikivie, *Axion cosmology*, Axions (2008), 19–50.
- [62] Yoshiaki Sofue, *Grand rotation curve and dark-matter halo in the milky way galaxy*, Publications of the Astronomical Society of Japan **64** (2012), no. 4, 75.
- [63] Peter Svrcek and Edward Witten, *Axions in string theory*, Journal of High Energy Physics **2006** (2006), no. 06, 051–051.
- [64] I. I. Tkachev, *Fast radio bursts and axion miniclusters*, JETP Letters **101** (2015), no. 1, 1–6.
- [65] Alejandro Vaquero, Javier Redondo, and Julia Stadler, *Early seeds of axion miniclusters*, Journal of Cosmology and Astroparticle Physics **2019** (2019), no. 04, 012–012.
- [66] David Wands, Oliver F. Piattella, and Luciano Casarini, *Physics of the cosmic microwave background radiation*, Astrophysics and Space Science Proceedings (2016), 3–39.
- [67] Olivier Wantz and E. P. S. Shellard, *Axion cosmology revisited*, Physical Review D **82** (2010), no. 12.
- [68] Steven Weinberg, *The cosmological constant problem*, Rev. Mod. Phys. **61** (1989), 1–23.
- [69] D Zaritsky, E W Olszewski, R A Schommer, R C Peterson, and M Aaronson, *Velocities of stars in remote galactic satellites and the mass of the galaxy*, Astrophysical Journal; (USA) **345** (1989).